

# Comparing 1-year GUMICS–4 simulations of the Terrestrial Magnetosphere with Cluster Measurements

G. Facskó<sup>1,2,3</sup>, D. G. Sibeck<sup>2</sup>, I. Honkonen<sup>4</sup>, J. Bór<sup>5</sup>, G. Farinas Perez<sup>2,3\*</sup>,  
A. Tímár<sup>1</sup>, Y. Y. Shprits<sup>6,7</sup>, L. Degener<sup>4†</sup>, P. Peitso<sup>8‡</sup>, E. I. Tanskanen<sup>8</sup>,  
C. R. Anekallu<sup>9</sup>, J. Kalmár<sup>5</sup>, S. Szalai<sup>5,10</sup>, Á. Kis<sup>5</sup>, V. Wesztergom<sup>5</sup>,  
N. A. Aseev<sup>6,7</sup>

<sup>1</sup>Wigner Research Centre for Physics, Budapest, Hungary

<sup>2</sup>NASA Goddard Space Flight Center, Greenbelt, Maryland, USA

<sup>3</sup>the Catholic University of America, Washington DC, USA

<sup>4</sup>Finnish Meteorological Institute, Helsinki, Finland

<sup>5</sup>Research Centre for Astronomy and Earth Sciences, Sopron, Hungary

<sup>6</sup>Helmholtz Centre Potsdam, GFZ German Research Centre for Geosciences, Potsdam, Germany

<sup>7</sup>Institute for Physics and Astronomy, University of Potsdam, Potsdam, Germany

<sup>8</sup>Aalto University, School of Electrical Engineering, Espoo, Finland

<sup>9</sup>UCL Department of Space & Climate Physics, Mullard Space Science Laboratory, Dorking, UK

<sup>10</sup>University of Miskolc, Department of Geophysics, Miskolc, Hungary

## Key Points:

- The GUMICS–4 code provides realistic ion plasma moments and magnetic field in the solar wind and the outer magnetosheath.
- The code [...] predicts [...] realistic bow shock locations [...].
- An inner magnetosphere model should be added to the code to increase the accuracy of the simulation in inner magnetosphere.

\*Now at University of Miami, Electrical and Computer Engineering Department, Miami, Florida, USA

†Now private individual, Hannover, Germany

‡Now at Aurora Propulsion Technologies, Espoo, Finland

Corresponding author: Gábor Facskó, [gabor.i.facsko@gmail.com](mailto:gabor.i.facsko@gmail.com)

23      **Abstract**

24      We compare the predictions of the GUMICS-4 global magnetohydrodynamic  
 25      model for the interaction of the solar wind with the Earth's magnetosphere  
 26      to Cluster-3 measurements over the course of one year, from January 29, 2002  
 27      to February 2, 2003. In particular, we compare [...] the north/south com-  
 28      ponent of the magnetic field ( $B_z$ ), the component of the velocity along the  
 29      Sun-Earth line ( $V_x$ ), and the plasma density as determined from a top hat  
 30      plasma spectrometer and the spacecraft's potential. We select intervals in the  
 31      solar wind, the magnetosheath and the magnetosphere where these instruments [...]  
 32      provided good quality data and the **model correctly predicts the region in which**  
 33      **the spacecraft is located**. We determine the location of the bow shock, the magnetopause  
 34      and the neutral sheet **from** the spacecraft measurements and compare their **locations**  
 35      **to those predicted by the simulation.**

36      The GUMICS-4 **model** provides quite good results in the solar wind however its  
 37      accuracy is **worse** in the magnetosheath. The simulation results are not realistic in the  
 38      magnetosphere. The bow shock location is predicted well however the magnetopause lo-  
 39      cation is less accurate. The neutral sheet positions are located quite well thanks to the  
 40      special solar wind conditions. [...]

41      **1 Introduction**

42      One of the most cost-effective way to study the interaction of the solar wind **with**  
 43      planetary magnetospheres (or predict the conditions **in** near-Earth space) is **modeling**  
 44      **this complex system** using a [...] magnetohydrodynamic (MHD) code. In the past,  
 45      several [...] parallelized [...] codes were developed, which are used and applied to fore-  
 46      cast the cosmic environment of the Earth; such as the Lyon-Fedder-Mobarry [LFM; *Lyon*  
 47      *et al.*, 2004] code, **the Grid Agnostic MHD for Extended Research Applications**  
 48      [**GAMERA**; *Zhang et al.*, 2019], the Open Geospace General Circulation Model [OpenG-  
 49      GCM; *Raeder et al.*, 2008], the Block-Adaptive-Tree-Solarwind-Roe-Upwind-Scheme [BATS-  
 50      R-US; *Powell et al.*, 1999; *Tóth et al.*, 2012]. In Europe only three global MHD codes  
 51      were developed: the Grand Unified Magnetosphere–Ionosphere Coupling Simulation [GUMICS-4;  
 52      *Janhunen et al.*, 2012], the Computational Object Oriented Libraries for Fluid Dynam-  
 53      ics [COOLFluiD; *Lani et al.*, 2012] and the 3D resistive magnetohydrodynamic code Gor-  
 54      gon [*Chittenden et al.*, 2004; *Ciardì et al.*, 2007]. The COOLFluiD is a general-purpose

plasma simulation tool. The Gorgon code was developed **to study** high energy, collisional plasma interactions and has been adapted to simulate planetary magnetospheres and their interaction with the solar wind [Mejnertsen *et al.*, 2016, 2018]. **Neither Gorgon nor COOLfluid have an ionospheric solver.** [...] **Almost all of** these codes are available at the Community Coordinated Modelling Center (CCMC; <http://ccmc.gsfc.nasa.gov/>) hosted by the NASA Goddard Space Flight Center (GSFC) **or** the Virtual Space Weather Modelling Centre (VSWMC; <http://swe.ssa.esa.int/web/guest/kul-cmpa-federated>; **re-**  
**quires registration for the European Space Agency (ESA) Space Situational Awareness (SSA) Space Weather (SWE) portal**) hosted by the KU Leuven [Poedts *et al.*, 2020]. **A comparison of** the simulation results **with** spacecraft and ground-based measurements is necessary to understand the abilities and features of the developed tools. **A statistical study using long term global MHD runs for validation** [...] **of the codes seems is needed. Because** [...] providing long simulations **are** costly and time consuming [...], only a few studies **have been done, almost all for periods much less than a year except Liemohn *et al.* [2018].**

*Guild et al.* [2008a,b] launched two months of LFM runs and compared the plasma sheet properties in the simulated tail with the statistical properties of six years Geotail magnetic field and plasma observations [Kokubun *et al.*, 1994; Mukai *et al.*, 1994]. The LFM successfully reproduced the global features of the global plasma sheet in **a statistical sense**. However, there were some differences. The sheet was too cold, too dense and the bulk flow was faster than the observed plasma sheet [Kokubun *et al.*, 1994; Mukai *et al.*, 1994]. The LFM overestimated the ionospheric transpolar potential. The transpolar potential correlated with the speed of the plasma sheet flows. Equatorial maps of density, thermal pressure, thermal energy and velocity were compared. The LFM overestimated the plasma sheet density close to the Earth, the temperature by a factor of  $\sim 3$  **and** the global average flow speed by a factor of  $\sim 2$ . The LFM reproduced many of the climatological features of the Geotail data set. The low-resolution model underestimated the occurrence of the fast earthward and tailward flows. Increasing the simulation resolution resulted in the development of fast, busty flows. **These flows influenced the statistics and contributed to a better agreement between simulations and observations.**

*Zhang et al.* [2011] [...] studied the statistics of magnetosphere-ionosphere (MI) coupling **using Guild et al.** [2008a]'s LFM simulation above. The polar cap po-

tential and the field aligned currents (FAC), the downward Poynting flux and the vorticity of the ionospheric convection were compared with observed statistical averages and the Weimer05 empirical model [Weimer, 2005]. The comparisons showed that the LFM model produced quite accurate average distributions of the Region 1 (R1) and Region 2 (R2) currents. The ionospheric **R2** currents in the MHD simulation seemed to **originate** from the diamagnetic ring current. The average LFM **R1** and **R2** currents were **small** compared with the values from the Weimer05 model. The average **Cross Polar Cap Potential (CPCP)** was higher in the LFM simulation than the measurements of the SuperDARN and the Weimer05 model. The average convention pattern was quite symmetric in the LFM simulation against the SuperDARN measurements and the Weimer05 model. The SuperDARN measurements and the Weimer05 model had **a** dawn-dusk asymmetry. In the LFM model, more Poynting flux flowed into the polar region ionosphere than in the Weimer05 model. It was the consequence of the larger CPCP in the LFM simulation. The larger CPCP allowed **a** higher electric field in the polar region. The statistical dependence of the high-latitude convection patterns on Interplanetary Magnetic Field (IMF) clock angle was similar to the SuperDARN measurements [Sofko *et al.*, 1995] and the Weimer05 model. The average ionospheric field-aligned vorticity showed good agreement on the dayside. However, the LFM model gave **a** larger nightside vorticity than SuperDARN measurements because the Pedersen conductance on the night side ionosphere was too low.

*Wiltberger et al.* [2017] studied the structure of [...] high latitude field-aligned current patterns using three resolutions of the LFM global MHD code and the Weimer05 empirical model [Weimer, 2005]. The studied period was a month long and contained two high-speed streams. Generally, the patterns agreed well with results obtained from the Weimer05 computing. As the resolution of the simulations increased, the currents became more intense and narrow. The ratio of the Region 1 (R1), the Region 2 (R2) currents and the R1/R2 ratio increased when the simulation resolution increases. However, both the R1 and R2 currents were smaller than the predictions of the Weimer05 model. This effect led to a better agreement of the LFM simulation results with the Weimer 2005 model results. The CPCP pattern became concentrated in higher latitudes because of the stronger R2 currents. The relationship of the CPCP and the R1 looked evident at higher resolution of the simulation. The LFM simulation could have reproduced the statistical features of the field aligned current (FAC) patterns.

121        *Hajducek et al.* [2017] simulated the month (**January,2005**) using the Space Weather  
122        Modelling Framework [SWMF; *Tóth et al.*, 2005] and the OMNI solar wind data (<https://omniweb.gsfc.nasa.gov/>)  
123        as input. The simulations were **compiled** with and without **an** inner magnetosphere model  
124        and using two different grid resolutions. The model was very good in predicting the **ring**  
125        currents [...] [SYM-H; <http://wdc.kugi.kyoto-u.ac.jp/aeasy/asy.pdf>; *Iyemori*, 1990]. The  
126         $K_p$  index (that measures the general magnetospheric convention and the auroral currents  
127        [*Bartels et al.*, 1939; *Rostoker*, 1972; *Thomsen*, 2004]) was predicted well during storms  
128        however the index was **overestimated** during quiet time periods. The AL index (that  
129        describes the westward electro jet of the surface magnetic field introduced by *Davis and*  
130        *Sugiura* [1966]) was predicted reasonably well **on** average. However the model reached  
131        the highest negative AL value less often **it was reached in the** observations because  
132        the model captured the structure of the auroral zone currents poorly. The overpredicting  
133        of  $K_p$  index during quiet times might have had the same reason because that index  
134        was also sensitive **to** auroral zone dynamics. The SWMF usually over predicted the CPCP.  
135        These results were not sensitive to grid **resolutions, with the except of** the AL in-  
136        dex, **whitch** reached the highest negative value more often when the grid resolution was  
137        higher. Switching off of the inner magnetosphere model had **a negative effect on** the  
138        accuracy of all quantities mentioned above, except the CPCP.

139        In this paper, the Cluster SC3 measurements are compared directly to a previously  
140        made 1-year long GUMICS–4 simulation in the solar wind, magnetosheath and the mag-  
141        netosphere along the Cluster SC3 orbit saved from the simulation results and measured  
142        by the spacecraft [*Facskó et al.*, 2016]. **In this paper these parameters, namely the**  
143         $B_z$ , **the north/south component of the magnetic field in GSE coordinates, the**  
144        **solar wind velocity GSE X component ( $V_x$ ) and the solar wind density  $n$  are**  
145        **compared to the Cluster SC3 measurements as well as the location of the bow**  
146        **shock, magnetopause and the neutral sheet. These parameters are selected**  
147        **because [...]  $B_z$  controls the magnetosphere, [...]  $V_x$  is the main component**  
148        **of the solar wind velocity [...] and [...]  $n$  is the ion plasma momentum that**  
149        **is the easiest to calculate; furthermore more instruments could determine it**  
150        **(see Section 2.2).** The structure of this paper is as follows. Section 2 describes the GUMICS–4  
151        code, the 1-year simulation and **the considered measurements of the Cluster space**  
152        **mission.** Section 3 gives comparisons between the simulations and observations. Results  
153        of the comparison are discussed in Section 4. Finally, Section 5 contains the conclusions.

154        **2 The GUMICS–4 products and Cluster measurements**

155        Here we use two [...] very different [...] time series. The first type is derived from  
 156        a previously 1-year **run of the GUMICS–4 simulation** [Facsikó *et al.*, 2016]. The sec-  
 157        ond **time series were** measured by the magnetometer, ion plasma and electric field in-  
 158        struments of the Cluster reference spacecraft.

159        **2.1 The GUMICS–4 code**

160        The GUMICS–4 has two coupled simulation domains, the magnetospheric domain  
 161        outside of  $3.7 R_E$  radius **sphere** around the Earth and a coupled ionosphere **module**  
 162        **containing 2D height-integrated model of ionosphere**. The GUMICS–4 is not a  
 163        parallel code however it **has been** extensively used for studying the energy propagation  
 164        processes from the solar wind to the magnetosphere through the magnetopause and other  
 165        features [Janhunen *et al.*, 2012, see the references therein]. The code has also been ap-  
 166        plied **to study** forced reconnection in the tail [Vörös *et al.*, 2014]. Recently, **several**  
 167        **hundred** synthetic two hours duration GUMICS–4 simulation **runs** were made to com-  
 168        pare the simulation results to empirical formulas [Gordeev *et al.*, 2013]. The agreement  
 169        was quite **good in general, but** the diameter of the magnetopause [...] in the sim-  
 170        ulation **deviated significantly from** observations in the tail. The [...] GUMICS–4  
 171        **simulation magnetotail** was smaller than **what the** spacecraft observed and measured.  
 172        A 1-year long simulation was made using the GUMICS–4 code [Facsikó *et al.*, 2016]. Ju-  
 173        usola *et al.* [2014] compared the ionospheric currents, fields and the [...] CPCP in the  
 174        simulation **to observations from the** Super Dual Auroral Radar Network (SuperDARN)  
 175        radars [Greenwald *et al.*, 1995] and CHAMP spacecraft [Reigber *et al.*, 2002] field aligned  
 176        currents (FAC) measurements [Juusola *et al.*, 2007; Ritter *et al.*, 2004]. The [...] CPCP,  
 177        [...] the FAC and other currents could not be reproduced properly. The possible cause  
 178        of this **poor** agreement could be **due to low resolution in inner magnetosphere**  
 179        **and/or** the lack of **an** inner magnetosphere model **incorporating the physics in this**  
 180        **region**. This **hypothesis** is supported by the result of Haiducek *et al.* [2017]. Haiducek  
 181        *et al.* simulated only a month-long period using a different spatial resolution and [...]  
 182        tested the code **with** the inner magnetosphere model of the SWMF **switched off** for  
 183        a special run. This run without **an** inner magnetosphere model made it clear that only  
 184        the CPCP parameter of the simulation agreed quite well with the measurements. This  
 185        fact explained why the agreement between the Cluster SC3 and the GUMICS-4 simu-

lations was so good as described by *Lakka et al.* [2018a,b] based on the CPCP in GUMICS–4 simulations. *Kallio and Facskó* [2015] determined **plasma and magnetic field** parameters along the **lunar** orbit **from** the *Facskó et al.* [2016]’s global MHD simulations. The [...] parameters differed significantly in the geotail **indicating a need for** future studies. *Facskó et al.* [2016] determined the footprint of [...] Cluster SC3 using the 1-year simulation and the Tsyganenko T96 empirical model [*Tsyganenko*, 1995]. [...] The agreement of the footprint **was** better in the Northern Hemisphere. The GUMICS–4 tail **was** shorter in the simulations than the observations. [...]

A 1-year global MHD simulation was produced with the GUMICS–4 code using the OMNI solar wind data from January 29, 2002 to February 2, 2003 as input [*Facskó et al.*, 2016]. The creation and analysis of the simulation was wased on a workpackage of the European Cluster Assimilation Technology (ECLAT) project ([https://cordis.europa.eu/result/rcn/165813\\_en.html](https://cordis.europa.eu/result/rcn/165813_en.html); <http://www.eclat-project.eu/>). The GUMICS-4 is a serial code [*Janhunen et al.*, 2012] hence the 1-year simulation was made in 1860 independent runs. This interval covered 155 Cluster SC3 orbits and each orbit lasted 57 hours. The FMI supercomputer **at the time** had 12 **cores** on each node hence the 57 hours were divided into 4.7 hours simulation time with one hour initialisation period. Each **sub-interval** used its own **individual** average Geocentric Solar Ecliptic (GSE) IMF magnetic field X component  $B_x$  component and dipole tilt angle. All data gaps **in solar wind** were **interpolated linearly**. If the data gap of the input file was at the beginning (or the end) **of the interval then** the first (or last) good data **from** the input file was used to fill the gap. The initialisation of each **simulation run** was made using constant values. These values were the first valid data of the input file repeated 60 times (60 minutes) in the input file of the sub-interval. The simulation results were saved [...] every five minutes. Various simulation parameters, for example, the density, particle density, temperature, magnetic field, solar wind velocity (29 different quantities) were saved from the simulation results along the Cluster reference spacecraft’s **orbit** in the GSE coordinates. [...]

## 2.2 The Cluster SC3 measurements

The Cluster-II spacecraft of the European Space Agency (ESA) were launched in 2000 and study the geospace [...] [*Credland et al.*, 1997; *Escoubet et al.*, 2001]. The four spacecraft form a tetrahedron **in space** however here we use only the measurements

of the reference spacecraft, [...] Cluster SC3. The spacecraft were stabilised [...] and their period is  $\sim 4$  s. Hence, the **intrinsic time** resolution of the plasma instruments is 4 s and we use 4 s averaged magnetic field data. The **highest** resolution of the Cluster FluxGate Magnetometer (FGM) magnetic field instrument is 27 Hz [Balogh *et al.*, 1997, 2001]. The ion plasma data **are** provided by the Cluster Ion Spectrometry (CIS) Hot Ion Analyser (HIA) sub-instrument [Reme *et al.*, 1997; Rème *et al.*, 2001]. The CIS HIA instrument is calibrated using the Waves of HIgh frequency Sounder for Probing the Electron density by Relaxation (WHISPER) wave instrument onboard Cluster [Décréau *et al.*, 2001; Trotignon *et al.*, 2010; Blagau *et al.*, 2013, 2014]. **The results of these calibrations can appear** as sudden non-physical jumps in the CIS HIA data. The CIS HIA had different modes to measure in the solar wind and the magnetosphere. When the instrument switched from **one** mode to another mode it appeared as a non-physical **jumps also appear** in the **measurements** [...]. These features **impair** the accuracy of [...] data **analyses**.

We protect our results from these non-physical jumps [...] using a density determination based on different principles. We use the spacecraft potential of the Electric Field and Wave Experiment [EFW ; Gustafsson *et al.*, 1997, 2001] to determine the electron density. This quantity can be calculated using the empirical density formula

$$n_{EFW} = 200(V_{sc})^{-1.85}, \quad (1)$$

where  $n_{EFW}$  is the calculated density and  $V_{sc}$  is the Cluster EFW spacecraft potential [Trotignon *et al.*, 2010, 2011]. The EFW and the WHISPER were used for the calibration of the CIS HIA and the Plasma Electron and Current Experiment [PEACE; Johnstone *et al.*, 1997; Fazakerley *et al.*, 2010a,b]. Both instruments were still working onboard all Cluster spacecraft. Their stable operation reduced the number of data **gaps**, **and it also** made the data analysis easier.

### 3 Comparison of measurements to simulation

The [...] parameters **saved** from the GUMICS–4 simulations and the Cluster SC3 magnetic field, solar wind velocity and density measurements are compared in **different regions, namely** the solar wind, magnetosheath and magnetosphere using cross correlation calculation. The **temporal** resolution of the simulated Cluster orbit data is mostly five minutes because the **results of the simulations** are saved [...] every five

248 minutes [Facsikó *et al.*, 2016]. However, the time difference between points **can** be more  
 249 than five minutes at the boundary of the subintervals, because the length of **the** sim-  
 250 ulation intervals is determined in minutes. To facilitate analysis of the simulation results,  
 251 all simulation data were interpolated to one minute resolution. This method does not  
 252 provide extra information to the cross correlation calculation. The data gaps are elim-  
 253 inated using **linear** interpolation [...] and extrapolation when the gap is at the start  
 254 or the end of the selected interval. The spin resolution (4 s) of Cluster SC3 magnetic field  
 255 measurements is averaged over one minute around ( $\pm 30\text{ s}$ ) the time stamps of the saved  
 256 data.

257 For the correlation calculation, intervals are selected carefully in the solar wind (**see**  
 258 **Section 3.1**), the magnetosheath (**see Section 3.2**), the dayside and the night side mag-  
 259 netosphere (**see Section 3.3**). In these intervals, the parameters did not vary a lot and  
 260 **we require** neither [...] Cluster nor the virtual probe **to cross** any boundaries. To  
 261 compare [...] the  $B_z$  magnetic field,  $V_x$  solar wind speed and the  $n_{CIS}$  and the  $n_{EFW}$   
 262 curves we [...] cross **correlate** selected intervals. [...] We carefully examine **such** cases  
 263 and remove [...] intervals **which are too short for the  $\pm 60$  minutes correlation**  
 264 **calculation** (shorter than four hours) [...] and large data gaps from the correlation  
 265 calculation. [...] Those intervals are also neglected where the plasma instrument has  
 266 a calibration error or **a change in its recording mode as it moves from the mag-**  
 267 **netosphere to solar wind** (for example). The electron density is also calculated using [...]  
 268 Equation 1 and [...] **correlated** [...]. We want to avoid **the** calibration errors and sud-  
 269 den non-physical jumps mentioned previously. The **correlation results for the den-**  
 270 **sity derived from the electric field potential** results do not differ significantly **from**  
 271 **those for the top hat plasma instrument**, however the  $n_{EFW}$  does not have any  
 272 mode change and it is applicable in the magnetosphere too (against the CIS HIA instru-  
 273 ment).

### 274 3.1 Solar wind

275 We use OMNI IMF and solar wind velocity, density and temperature data as in-  
 276 put **to** the simulation. **There is a reason why we** compare **parameters in the** so-  
 277 **lar wind region in the simulation and the measurements.** The IMF X component can-  
 278 not be given to the GUMICS-4 as input [Janhunen *et al.*, 2012; Facsikó *et al.*, 2016]. How-  
 279 ever, the magnetic field of the solar wind has **an** X component in the simulations. Ad-

ditionally, the solar wind structure might change from the simulation domain boundary at  $+32 R_E$  to the sub-solar point of the terrestrial bow shock where all OMNI data is shifted. Almost the same solar wind **time** intervals are used as in [...] Table 1 of *Facskó et al. [2016]*. The number of these intervals is small because [...] Cluster fleet instruments were calibrated in 2002, just after **launch** (Table 1). Hence we do not have a satisfactory ion plasma data coverage for this year. Additionally, to improve the accuracy of the correlation calculation (see below) we delete the intervals that were too short (shorter than five hours) or the CIS HIA instrument changed its mode. The Cluster fleet is located in the solar wind only from December to May and only for a couple of hours during each orbit near [...] apogee. We double check whether the Cluster SC3 stays in the solar wind in both the simulation and reality. We also check the omnidirectional CIS HIA ion spectra on the Cluster Science Archive (CSA; <https://www.cosmos.esa.int/web/csa/csds-quicklook-plots>). **The spectra must contain one narrow band in the solar wind region.** Hence 17 intervals are left in the solar wind to study (Figure 1).

The selected intervals **occur for** quiet solar wind conditions (Figure 2). The GUMICS-4 simulation results have five minutes resolution and the Cluster SC3 measurements have one minute resolution (Figure 3). The measurements vary significantly. In spite of the quiet conditions the solar wind density often changes and deviates from the simulation. [...] Figure 4c **shows that** both densities deviate significantly. The CIS HIA density deviation is larger as [...] expected **given** the complexity and the large number of working modes of the CIS instrument. The magnetic field and the solar wind velocity fit better. [...] Figure 5a **shows that** the correlation of the magnetic fields is very good; furthermore on Figure 5c, 5e, 5f the correlation of the solar wind velocity and density is excellent (Table 1). The time shift on Figure 5b, Figure 5d, Figure 5f is about five minutes for the magnetic field and the CIS data. On Figure 5h for the EFW data the time shift is **less stable**. It is not **as well** determined as **in case of** the other parameters.

### 3.2 Magnetosheath

The Cluster SC3 spent only a little time in the solar wind from December, 2002 to May, 2003. However, the [...] spacecraft **enters** the magnetosheath each orbit (Figure 6). We selected intervals when the value of the magnetic field is around 25 nT. The field should be fluctuating because of the turbulent **deflected** flow of the **shocked** solar wind [...] the **temperature should be greater than that in the solar wind** [...].

312 The velocity should decrease to values ranging from 100-300 km/s. The density  
 313 of the plasma should increase and reached values of  $10\text{-}20 \text{ cm}^{-3}$ . The narrow band  
 314 on the omnidirectional CIS HIA ion spectra from the CSA (<https://www.cosmos.esa.int/web/csa/csds-quicklook-plots>) widens from the solar wind to the magnetosheath. 15–30 minutes  
 315 from each bow shock crossing we considered the Cluster SC3 to have entered into  
 316 the magnetosheath. At the inner magnetopause boundary of the magnetopause the  
 317 flow speed [...] and the density drop. The magnetic field strength increases and the  
 318 magnetic field becomes less turbulent than in the magnetosheath. The wide band on  
 319 the omnidirectional CIS HIA ion spectra disappears. 15–30 minutes before the appear-  
 320 ance of these indicators of the magnetopause crossing our intervals end. All inter-  
 321 vals contain large data gaps, non-physical jump in instrument modes [...] or lasting  
 322 less than four hour are removed. Hence 74 intervals considered in our final selection (Ta-  
 323 ble 2).

325 All intervals have quiet upstream (or input) solar wind conditions (Figure 7). Inspite  
 326 of our selected [...] magnetic field and [...] plasma parameters and the calculated em-  
 327 pirical density indicate that they vary significantly stronger than in the solar wind in-  
 328 tervals (Figure 8). The deviation between the simulated and the observed data is also  
 329 larger in this region [...]. The scatter plots of the magnetic field, plasma flow speed  
 330 and the densities show that these parameters agree well, but with greater vari-  
 331 ation than the scatter plots for the solar wind (Figure 9a, 9b, 9c). The correlation of  
 332 the simulated and the observed data is good for the magnetic field (Figure 10a), very  
 333 good for the ion plasma moments and the calculated density (Figure 10c, 10e, 10g). The  
 334 timeshift of the magnetic field is within five minutes mostly (Figure 10b) however the  
 335 timeshift of the ion plasma moments is scattered (Figure 10d, 10f). The timeshift of the  
 336 calculated EFW density seems to be more stable (Figure 10h). Generally, the GUMICS–4  
 337 is less accurate in the magnetosheath than in the solar wind. The modelled mag-  
 338 netic field is closer to the observations than the modelled plasma parameters  
 339 are. The calculated empirical EFW density ( $n_{EFW}$ ) fits better than the CIS HIA den-  
 340 sity ( $n_{CIS}$ ).

### 341 3.3 Magnetosphere

342 To select intervals in the magnetosphere we looked for the CIS HIA omnidirectional  
 343 ion flux spectrum. Where the band of the hot magnetosheath ion population (dis)appeared,

344 the magnetosphere started/finished. The **plasma density decreases toward zero**, the  
 345 magnetic field **strength is large**. We left 15–30 min after/before the magnetopause transi-  
 346 tion to **identify magnetosphere intervals**. This way we found 132 intervals in the mag-  
 347 netosphere (Table 3) using Cluster SC3 measurements. [...] Cluster SC3 spends con-  
 348 siderable time in the magnetosphere (Figure 11).

349 Here we show neither any correlation calculation nor comparison plot. In the mag-  
 350 netosphere the GUMICS–4 does not work well. Neither the magnetic field nor the plasma  
 351 moments nor the  $N_{EFW}$  fit well. The solar wind velocity does not reach zero in the sim-  
 352 ulation. Instead, the solar wind enters to the night side magnetosphere. The solar wind  
 353 CIS HIA ion plasma density and the calculated density from spacecraft potential increase  
 354 closer to the Earth (plasmasphere). The GUMICS–4 density is low there. We calculated  
 355 the dipole field in GSE using Tsyganenko geotool box [Tsyganenko, 1995] and substracted  
 356 from both the observed and the simulated magnetic field  $B_z$  data. The correlation of these  
 357 corrected magnetic field measurements and simulations is very low too.

### 358 3.4 Bow shock, magnetopause, neutral sheet

359 77 intervals are selected when [...] Cluster SC3 crossed the terrestrial bow shock  
 360 once or multiple times (**Table 6**). When the spacecraft crosses the bow shock **inbound**  
 361 the magnitude of the magnetic field and the solar wind density increases **by a factor**  
 362 **of 4–5 times** (from 5 nT or  $5 \text{ cm}^{-3}$ , respectively), the solar wind speed drops from 400–  
 363 600 km/s to 100–300 km/s; furthermore the narrow band on the omnidirectional Clus-  
 364 ter CIS HIA ion spectra [...] widens. The Cluster measurements are 1-min averaged  
 365 **whereas** the GUMICS–4 simulations have 5-min resolution. Hence all bow shock tran-  
 366 sitions of the virtual spacecraft are slower and smoother. Additionally, the multiple bow  
 367 shock transitions are not visible in the GUMICS simulations. The code reacts slowly for  
 368 such sudden changes. The magnetic signatures fit better than the calculated plasma mo-  
 369 ments. The jump of the ion plasma parameters and the derived Cluster EFW density  
 370 of the simulations are shifted to the measurements. Generally, the density and the ve-  
 371 locity of the simulations seem to be less accurate than the magnetic field of the simu-  
 372 lations.

373 54 intervals are selected around magnetopause crossings [...] (**Table 7**). When  
 374 the spacecraft crosses the magnetopause **inbound** the magnitude of the magnetic field

increases, the solar wind speed drops from 100–300 km/s to zero, the plasma density becomes zero; furthermore the wide band on the omnidirectional Cluster CIS HIA ion spectra disappears. [...] The location of the magnetopause is well determined by the Cluster SC3 measurements. However, it is very difficult to identify the magnetopause crossings in the simulation data. [...] The magnetopause crossings very often cannot be seen in the simulations. Or when the magnetopause crossings are clearly identified in both simulations and spacecraft measurements the events are shifted. The accuracy of the model is lower for the dayside magnetopause locations.

Nine intervals are chosen around Cluster SC3 neutral sheet crossings (Figure 12; Table 8). The neutral **sheet** locations **are** determined using the results of the Boundary Layer Identification Code (BLIC) Project [Facskó *et al.*, in preparation]. The BLIC code determines the neutral sheet crossing Cluster FGM magnetic field measurements using Wang and Xu [1994]’s method. When the solar wind speed is almost zero; furthermore the CIS HIA density and the EFW calculated density are almost zero too; finally the GSE Z component of the magnetic field changes is a sign of the code indicated neutral sheet crossing (Figure 19; red and blue curves). [...] The neutral sheet crossings are visible very well in the GUMICS simulations (Figure 19; black curves). For five events (from nine Cluster SC3 crossings) the GUMICS–4 also provides similar smoothed parameters and change of sign of the  $B_z$  component. This is a **outstanding** result because the tail in the GUMICS–4 simulations is significantly smaller than the observed reality [Gordeev *et al.*, 2013; Facskó *et al.*, 2016]; furthermore the solar wind enters the tail in MHD simulations generally [Kallio and Facskó, 2015].

## 4 Discussion

The agreement of [...]  $B_z$ ,  $V_x$  and  $n_{EFW}$  **in the solar wind** with the similar GUMICS simulation **predictions** is very good (Figure 4a, 4b, 4c, blue). The agreement of [...]  $n_{CIS}$  is worse (Figure 4c, red). It was expected because the  $n_{EFW}$  depends on the spacecraft potential provided by the EFW instrument. However, the CIS instrument has many modes for measuring the plasma parameters and it needs **periodic** calibration too. The correlation of the solar wind  $V_x$ ,  $n_{CIS}$  and  $n_{EFW}$  with the similar GUMICS simulation parameters is greater than 0.9 (Figure 5c, 5e, 5g). The correlation of the  $B_z$  is also greater than 0.8 (Figure 5a). [...] The **upstream boundary** of the GUMICS–4 code **lies** at  $32 R_E$  [Janhunen *et al.*, 2012], the nose of the terrestrial bow shock is at about

407     $20 R_E$ . If the solar wind speed is 400 km/s, then this spatial distance means less than  
 408    **a 5 minutes delay**, so it should not be visible **in the time delays from the cross cor-**  
 409    **relations**. 80% of the intervals support this theory but 20 % **do not**. In these cases, the  
 410    one-minute resolution  $B_z$ ,  $n_{CIS}$  or the  $n_{EFW}$  parameters have a sudden jump or vari-  
 411    ation that the simulation cannot follow, or the resolution of the simulation **output** (5 minutes)  
 412    is too small to see these variations. Therefore, the correlation calculation is not accu-  
 413    rate in these cases. Previously the OMNI data was compared to the Cluster data and  
 414    the Cluster measurements were compared to the GUMICS–4 [Facsikó *et al.*, 2016]. The  
 415    comparison suggests that the GUMICS–4 results should be similar **for** the OMNI data.  
 416    Furthermore, we calculate correlation functions in the solar wind, where there is no sig-  
 417    nificant perturbation of the input parameters in the simulation box. Therefore, we get  
 418    **the expected result** after comparing the two different correlation calculations.

419    In the magnetosheath we get worse agreement with the GUMICS simulation data  
 420    (Figure 9a, 9b, 9c). **While the parameters are correlated, the scatter is greater.**  
 421    The general reason **for** this larger uncertainty seems to be [...] **that the magnetosheath**  
 422    **is turbulent**. This phenomena explains the higher variations of the  $B_z$  magnetic field  
 423    on Figure 9a. The solar wind  $V_x$ ,  $n_{CIS}$  and  $n_{EFW}$  agree better than the magnetic field  
 424    component (Figure 9b, 9c). Here there is no deviation between the densities derived in  
 425    different ways ( $n_{CIS}$  and  $n_{EFW}$ ) on Figure 9c. Figure 10 seems to contradict these state-  
 426    ments above. The larger uncertainty of the  $B_z$  is visible on Figure 10a. However, that  
 427    correlation is still good on Figure 10b. The other parameters have larger ( $> 0.9$ ) cor-  
 428    relation in Figure 10c, 10e, 10g. However, the time shifts in Figure 10d, 10f, 10h seem  
 429    to be worse. Actually here the time shifts are worse because the shape of the time se-  
 430    ries in the magnetosheath looks very **smooth and similar hence there is not enough**  
 431    **points to get a sharp and large maximum correlation as the function of timeshift.**  
 432    **The difference between the minimum and the maximum of the correlation**  
 433    **is small comparing with the uncertainty of the calculation. The maximum,**  
 434    **the timeshift could be anywhere and the shape of the correlation vs. timeshift**  
 435    **function is often neither symmetric nor has only one local maximum.** Hence,  
 436    the correlation calculation provides larger time shifts for the ion plasma parameters and  
 437    the  $n_{EFW}$ .

438    In the magnetosphere the GUMICS–4 does not work well. [...] GUMICS–4 uses  
 439    a tilted dipole to describe the terrestrial magnetic field [Janhunen *et al.*, 2012]. After re-

440 moving the magnetic dipole from the magnetic field measurements of the Cluster SC3  
 441 and the simulation we get very low correlations and unacceptable time shifts (not shown).  
 442 [...] The tilted dipole is an insufficient description **of the inner magnetospheric mag-**  
 443 **netic field.** [...] The plasma **moments** and the  $n_{EFW}$  do not fit either. **The single**  
 444 **fluid, ideal MHD does not describe the inner magnetosphere well** therefore [...]  
 445  $V_x$  and [...]  $n$  in the simulations do not agree **with**  $V_x$ , [...]  $n_{CIS}$  and the  $n_{EFW}$  mea-  
 446 **sured by the Cluster SC3.** Within the  $3.7 R_E$  domain **ring current physics must be**  
 447 **added, as it has been** in other global MHD codes [for example *Tóth et al., 2012*].  
 448 This [...] can explain [...] the limited accuracy of the cross polar cap potential (CPCP)  
 449 and geomagnetic indices of the GUMICS simulations [*Juusola et al., 2014*]. The CPCP  
 450 [...] GUMICS **agrees well with** spacecraft measurements therefore this quantity could  
 451 be used for [...] simulation studies [*Lakka et al., 2018a*]. *Hajducek et al.* [2017] also [...]  
 452 **compared** [...] geomagnetic indices and the CPCP. The Space Weather Modelling Frame-  
 453 work (SWMF) was tested. When the inner magnetosphere model was switched off in the  
 454 simulation only the comparison of the simulated and observed CPCP was good. There-  
 455 fore, the reason of the discrepancy of the geomagnetic indices in the GUMICS simula-  
 456 tions must be the missing inner magnetosphere model.

457 **The reason of why simulation results and [...] measurements disagree**  
 458 **could be the code or the bad input parameters.** During the 1-year run the  
 459 **distributions of the OMNI solar wind magnetic field  $B_x$ ,  $B_y$ ,  $B_z$  components**  
 460 [...] ; **solar wind velocity  $V_x$ ,  $V_y$   $V_z$  components** [...] and the solar wind  $P$  dy-  
 461 **namic pressure** are calculated [...] from January 29, 2002 to February 2, 2003  
 462 in GSE reference frame. These distributions of the OMNI solar wind mag-  
 463 **netic field  $B_x$ ,  $B_y$ ,  $B_z$  components** were overplotted by red in Figure 13a, 13d, 13g, 13j  
 464 and Figure 16a, 16d, 16g, 16j; Figure 13b, 13e, 13h, 13k and Figure 16b, 16e, 16h, 16k;  
 465 furthermore Figure 13c, 13f, 13i, 13l and Figure 16c, 16f, 16i, 16l. These dis-  
 466 **dtributions of the OMNI solar wind velocity  $V_x$ ,  $V_y$ ,  $V_z$  components** were over-  
 467 plotted by red in Figure 14a, 14d, 14g, 14j and Figure 17a, 17d, 17g, 17j; Fig-  
 468 ure 14b, 14e, 14h, 14k and Figure 17b, 17e, 17h, 17k; furthermore Figure 14c, 14f, 14i, 14l  
 469 and Figure 17c, 17f, 17i, 17l. These distributions of the  $P$  solar wind pres-  
 470 **sure calculated from the OMNI solar wind parameters** were overplotted by  
 471 red in Figure 15a, 15b, 15c, 15d and Figure 18a, 18b, 18c, 18d. The intervals  
 472 when the GUMICS–4 simulations and the Cluster SC3 measurements dis-

473 agreed are collected for intervals in the solar wind (Table 4) and the mag-  
 474 netosheath (Table 5). The averaged shifted OMNI parameters of the poorly  
 475 agreeing intervals from the Tables 4 and 5 are saved. The distributions of the  
 476 OMNI parameters belonging to the bad simulation results are calculated for  
 477 the solar wind region (Figure 13, 14 and 15) and in the magnetosheath (Fig-  
 478 ure 16, 17 and 18).

479 **1.** In the solar wind the distributions of the OMNI  $B_x$ ,  $B_y$  and  $B_z$  can be  
 480 compared in Figure 13a, 13d, 13g, 13j; Figure 13b, 13e, 13h, 13k; fur-  
 481 thermore in Figure 13c, 13f, 13i, 13l.

- 482 (a) When the  $B_z$  disagrees in simulations and measurements in Figure 13a, 13b, 13c  
 483 the black and red distributions of the OMNI  $B_x$ ,  $B_y$  and  $B_z$  are not  
 484 similar [...] . The reason of these strange spikes is that there is only  
 485 one poorly correlated interval for the  $B_z$  in the solar wind according  
 486 to Table 4.
- 487 (b) When the  $V_x$  disagrees in simulations and measurements in Figure 13d, 13e, 13f  
 488 the black and red distributions of the OMNI  $B_x$ ,  $B_y$  and  $B_z$  are sim-  
 489 ilar [...] . The distributions do not agree perfectly because in Table 4  
 490 the number of the poorly correlated intervals is only six for the  $V_x$   
 491 component.
- 492 (c) When the  $n_{CIS}$  disagrees in simulations and measurements in Figure 13g, 13h, 13i  
 493 the black and red distributions of the OMNI  $B_x$ ,  $B_y$  and  $B_z$  are sim-  
 494 ilar [...] . The distributions do not agree perfectly because in Table 4  
 495 the number of the poorly correlated intervals is only 12 for the  $n_{CIS}$ .
- 496 (d) When the  $n_{EFW}$  disagrees in Figure 13j, 13k, 13l the black and red  
 497 distributions of the OMNI  $B_x$ ,  $B_y$  and  $B_z$  are similar [...] . The dis-  
 498 tributions do not agree perfectly because in Table 4 the number of  
 499 the poorly correlated intervals is only nine for  $n_{EFW}$ .

500 The values of the OMNI  $B_x$ ,  $B_y$  and  $B_z$  are not peculiar in the solar wind.

501 **2.** In the solar wind the distributions of the OMNI  $V_x$ ,  $V_y$  and  $V_z$  can be  
 502 compared in Figure 14a, 14d, 14g, 14j; Figure 14b, 14e, 14h, 14k; fur-  
 503 thermore in Figure 14c, 14f, 14i, 14l.

- 504 (a) When the  $B_z$  disagrees in Figure 14a, 14b, 14c the black and red dis-  
 505 tributions of the OMNI  $V_x$ ,  $V_y$  and  $V_z$  are not similar [...] . The rea-  
 506 son of these strange spikes is that there is only one poorly correlated  
 507 interval for the  $B_z$  in the solar wind according to Table 4.
- 508 (b) When the  $V_x$  disagrees in simulations and measurements in Figure 14d, 14e, 14f  
 509 the black and red distributions of the OMNI  $V_x$ ,  $V_y$  and  $V_z$  are sim-  
 510 ilar [...] . The distributions do not agree perfectly because in Table 4  
 511 the number of the poorly correlated intervals is only six for the  $V_x$   
 512 component.
- 513 (c) When the  $n_{CIS}$  disagrees in Figure 14g, 14h, 14i the black and red  
 514 distributions of the OMNI  $V_x$ ,  $V_y$  and  $V_z$  are similar [...] . The dis-  
 515 tributions do not agree perfectly because in Table 4 the number of  
 516 the poorly correlated intervals is only 12 for the  $n_{CIS}$ .
- 517 (d) When the  $n_{EFW}$  disagrees in simulations and measurements in Fig-  
 518 ure 14j, 14k, 14l the black and red distributions of the OMNI  $V_x$ ,  $V_y$   
 519 and  $V_z$  are similar [...] . The distributions do not agree perfectly be-  
 520 cause in Table 4 the number of the poorly correlated intervals is only  
 521 nine for the  $n_{EFW}$ .

522 The values of the OMNI  $V_x$ ,  $V_y$  and  $V_z$  are not peculiar in the solar wind.

523 **3. In the solar wind the distributions of the solar wind P calculated from**  
 524 **OMNI parameters can be compared in Figure 15a, 15b, 15c, 15d.**

- 525 (a) When the  $B_z$  disagrees in Figure 15a the black and red distributions  
 526 of the OMNI  $P$  are not similar [...] . The reason of these strange spike  
 527 is that there is only one poorly correlated interval for the  $B_z$  in the  
 528 solar wind according to Table 4.
- 529 (b) When the  $V_x$  disagrees in simulations and measurements in Figure 15b  
 530 the black and red distributions of the OMNI  $P$  are similar [...] . The  
 531 distributions do not agree perfectly because in Table 4 the number  
 532 of the poorly correlated intervals is only six  $V_x$  component.
- 533 (c) When the  $n_{CIS}$  disagrees in simulations and measurements in Figure 15c  
 534 the black and red distributions of the OMNI  $P$  are similar [...] . The  
 535 distributions do not agree perfectly because in Table 4 the number  
 536 of the poorly correlated intervals is only 12 for the  $n_{CIS}$ .

537 (d) When the  $n_{EFW}$  disagrees in simulations and measurements in Fig-  
 538 ure 15d the black and red distributions of the OMNI  $P$  are similar  
 539 [...] . The distributions do not agree perfectly because in Table 4 the  
 540 number of the poorly correlated intervals is only nine for the  $n_{EFW}$ .

541 The values of the OMNI  $P$  are not peculiar in the solar wind.

542 4. In the magnetosheath the distributions of the OMNI  $B_x$ ,  $B_y$  and  $B_z$  can  
 543 be compared in Figure 16a, 16d, 16g, 16j; Figure 16b, 16e, 16h, 16k; fur-  
 544 thermore in Figure 16c, 16f, 16i, 16l.

- 545 (a) When the  $B_z$  disagrees in simulations and measurements in Figure 16a, 16b, 16c  
 546 the black and red distributions of the OMNI  $B_x$ ,  $B_y$  and  $B_z$  are sim-  
 547 ilar [...] .
- 548 (b) When the  $V_x$  disagrees in simulations and measurements in Figure 16d, 16e, 16f  
 549 the black and red distributions of the OMNI  $B_x$ ,  $B_y$  and  $B_z$  are sim-  
 550 ilar [...] .
- 551 (c) When the  $n_{CIS}$  disagrees in simulations and measurements in Figure 16g, 16h, 16i  
 552 the black and red distributions of the OMNI  $B_x$ ,  $B_y$  and  $B_z$  are sim-  
 553 ilar [...] .
- 554 (d) When the  $n_{EFW}$  disagrees in Figure 16j, 16k, 16l the black and red  
 555 distributions of the OMNI  $B_x$ ,  $B_y$  and  $B_z$  are similar [...] .

556 The distributions agree quite well because in Table 5 the number of the  
 557 poorly correlated intervals 18, 50, 33 and 30 for the  $B_z$ , the  $V_x$ , the  $n_{CIS}$   
 558 and  $n_{CIS}$  components, respectively. The number of cases are higher and  
 559 the values of the OMNI  $B_x$ ,  $B_y$  and  $B_z$  are not peculiar in the magne-  
 560 tosheath.

561 5. In the magnetosheath the distributions of the OMNI  $V_x$ ,  $V_y$  and  $V_z$  can  
 562 be compared in Figure 17a, 17d, 17g, 17j; Figure 17b, 17e, 17h, 17k; fur-  
 563 thermore in Figure 17c, 17f, 17i, 17l.

- 564 (a) When the  $B_z$  disagrees in Figure 17a, 17b, 17c the balck and red dis-  
 565 tributions of the OMNI  $V_x$ ,  $V_y$  and  $V_z$  are similar [...] .
- 566 (b) When the  $V_x$  disagrees in simulations and measurements in Figure 17d, 17e, 17f  
 567 the black and red distributions of the OMNI  $V_x$ ,  $V_y$  and  $V_z$  are sim-  
 568 ilar [...] .

569 (c) When the  $n_{CIS}$  disagrees in Figure 17g, 17h, 17i the black and red  
 570 distributions of the OMNI  $V_x$ ,  $V_y$  and  $V_z$  are similar [...] .

571 (d) When the  $n_{EFW}$  disagrees in simulations and measurements in Fig-  
 572 ure 17j, 17k, 17l the black and red distributions of the OMNI  $V_x$ ,  $V_y$   
 573 and  $V_z$  are similar [...] .

574 The distributions agree quite well because in Table 5 the number of the  
 575 poorly correlated intervals 18, 50, 33 and 30 for the  $B_z$ , the  $V_x$ , the  $n_{CIS}$   
 576 and  $n_{CIS}$  components, respectively. The number of cases are higher and  
 577 the values of the OMNI  $V_x$ ,  $V_y$  and  $V_z$  are not peculiar in the magne-  
 578 tosheath.

579 6. In the magnetosheath the distributions of the solar wind P calculated  
 580 from OMNI parameters can be compared in Figure 18a, 18b, 18c, 18d.

581 (a) When the  $B_z$  disagrees in Figure 18a the black and red distributions  
 582 of the OMNI  $P$  are similar [...] .

583 (b) When the  $V_x$  disagrees in simulations and measurements in Figure 18b  
 584 the black and red distributions of the OMNI  $P$  are similar [...] .

585 (c) When the  $n_{CIS}$  disagrees in simulations and measurements in Figure 18c  
 586 the black and red distributions of the OMNI  $P$  are similar [...] .

587 (d) When the  $n_{EFW}$  disagrees in simulations and measurements in Fig-  
 588 ure 18d the black and red distributions of the OMNI  $P$  are similar  
 589 [...] .

590 The distributions do not agree perfectly because in Table 5 the num-  
 591 ber of the poorly correlated intervals is only 6, 12 and 9 for the  $V_x$ , the  
 592  $n_{CIS}$  and  $n_{CIS}$  components, respectively. The distributions agree quite  
 593 well because in Table 5 the number of the poorly correlated intervals  
 594 18, 50, 33 and 30 for the  $B_z$ , the  $V_x$ , the  $n_{CIS}$  and  $n_{CIS}$  components, re-  
 595 spectively. The number of cases are higher and the values of the OMNI  
 596  $P$  are not peculiar in the magnetosheath.

597 The inaccuracy of the GUMICS-4 simulations does not depend on the OMNI  
 598 parameters in the solar wind and magnetosheath regions. The same study  
 599 does not need to be done for the magnetosphere because the deviation of the

600 **measurements and the simulations is so large that it cannot be caused by the**  
 601 **wrong OMNI solar wind parameters.**

602 The bow shock positions agree in the GUMICS simulations and the Cluster SC3  
 603 measurements. However, the magnetopause locations do not fit **well** as the bow shock  
 604 in simulations and observations. In simulations the location of the magnetopause is de-  
 605 termined **from peaks in currents density, particle density gradient, or changes in flow**  
 606 **velocity** [Siscoe *et al.*, 2001; García and Hughes, 2007; Gordeev *et al.*, 2013, see refer-  
 607 ences therein]. In this paper the previously saved simulation parameters along the vir-  
 608 tual Cluster SC3 orbit are analysed. **The  $J_y$  current density component cannot be**  
 609 **calculated from only the Cluster SC3 measurements.** Therefore, the above men-  
 610 tioned methods cannot be applied. [...] This discrepancy of the magnetopause loca-  
 611 tion agrees with the results of Gordeev *et al.* [2013] and Facskó *et al.* [2016]. Gordeev *et al.*  
 612 [2013] compared synthetic GUMICS runs with **an empirical formula for** the magnetopause  
 613 locations. Facskó *et al.* [2016] used OMNI solar wind data as input and got the same re-  
 614 sult as Gordeev *et al.* [2013] and this paper. [...] The neutral sheets are visible in both  
 615 simulations and observations (Figure 19, Table 8). This experience is exceptional because  
 616 the night side magnetosphere of the GUMICS–4 simulations is small and twisted [Gordeev  
 617 *et al.*, 2013; Facskó *et al.*, 2016]. However, in these cases the IMF has no large  $B_y$  com-  
 618 ponent. From Facskó *et al.* [2016] we know that the GUMICS has normal long tail (or  
 619 night side magnetosphere) if the  $B_y$  is small.

## 620 5 Summary and conclusions

621 Based on the previously created 1-year long GUMICS–4 run global MHD simu-  
 622 lation results are compared with Cluster SC3 magnetic field, solar wind velocity and den-  
 623 sity measurements along the spacecraft orbit. Intervals are selected when the Cluster SC3  
 624 and the virtual space probe are situated in the solar wind, magnetosheath and the mag-  
 625 netosphere and their correlation are calculated. Bow shock, magnetopause and neutral  
 626 sheet crossings are selected and their visibility and relative position are compared. We  
 627 achieved the following results:

628 1. **In the solar wind the correlation coefficient of the  $B_z$ , the  $V_x$ , the  $n_{EFW}$**   
 629 **and the  $n_{CIS}$  are larger than 0.8, 0.9, 0.9 and 0.9, respectively. [...] The**

630 agreement of the  $B_z$ , the  $V_x$  and the  $n_{EFW}$  is very good, furthermore the agree-  
 631 ment of the  $n_{CIS}$  is also good.

632 **2. In the magnetosheath the correlation coefficient of the  $B_z$ , the  $V_x$ , the  
 633  $n_{EFW}$  and the  $n_{CIS}$  are larger than 0.6, 0.9, 0.9 and 0.9, respectively.**

634 [...] The agreement of the magnetic field component, the ion plasma moments  
 635 and the calculated empirical density is a bit worse than in the solar wind. The  $V_x$ ,  
 636 the  $n_{EFW}$  and the  $n_{CIS}$  fits better than the  $B_z$  component in the magnetosheath.  
 637 Their agreement is still good. The reason of the deviation is the turbulent behav-  
 638 ior of the slowed down and thermalised turbulent solar wind.

639 **3. In neither the dayside nor the nightside magnetosphere can the GUMICS-4 pro-  
 640 vide realistic results. The simulation outputs and the spacecraft measurement dis-  
 641 agree in this region. The reason of this deviation must be the missing coupled in-  
 642 ner magnetosphere model. The applied tilted dipole approach is not satisfactory  
 643 in the magnetosphere at all.**

644 **4. Disagreement between GUMICS-4 and observations does not seem to  
 645 be due to upstream solar wind.**

646 **5. The position of the bow shock and the neutral sheet agrees well in the simulations  
 647 and the Cluster SC3 magnetic field, ion plasma moments and derived electron den-  
 648 sity measurements in this study. The position of the magnetopause does not fit  
 649 that well. [...]**

650 The GUMICS-4 has [...] scientific and strategic importance for the European Space  
 651 Weather and Scientific community. This code developed in the Finnish Meteorological  
 652 Institute is the most developed and tested, widely used tool for modelling the cosmic en-  
 653 viroment of the Earth in the Europe. [...] An inner magnetosphere model should  
 654 be two way coupled to the existing configuration of the simulation tool to improve the  
 655 accuracy of the simulations.

656 **Acknowledgments**

657 The OMNI data were obtained from the GSFC/SPDF OMNIWeb interface at <http://omniweb.gsfc.nasa.gov>.  
 658 The authors thank the FGM Team (PI: Chris Carr), the CIS Team (PI: Iannis Dandouras),  
 659 the WHISPER Team (PI: Jean-Louis Rauch), the EFW Team (PI: Mats Andre) and the  
 660 Cluster Science Archive for providing FGM magnetic field, CIS HIA ion plasma and WHIS-  
 661 PER electron density measurements. Data analysis was partly done with the QSAS sci-

ence analysis system provided by the United Kingdom Cluster Science Centre (Imperial College London and Queen Mary, University of London) supported by the Science and Technology Facilities Council (STFC). Eija Tanskanen acknowledges financial support from the Academy of Finland for the ReSoLVE Centre of Excellence (project No. 272157). Gábor Facskó thanks Anna-Mária Vígh for improving the English of the paper. The authors thank Pekka Janhunen for developing the GUMICS–4 code; furthermore Minna Palmroth and Zoltán Vörös for the useful discussions. The work of Gábor Facskó was supported by mission science funding for the Van Allen Probes mission, the American Geophysical Union and the HAS Research Centre for Astronomy and Earth Sciences, Sopron, Hungary. For further use of the year run data, [...] **request the authors or** use the archive of the Community Coordinated Modelling Center (<https://ccmc.gsfc.nasa.gov/publications/posted>)

## 674 References

- 675 Balogh, A., M. W. Dunlop, S. W. H. Cowley, D. J. Southwood, J. G. Thomlinson,  
 676 K. H. Glassmeier, G. Musmann, H. Luhr, S. Buchert, M. H. Acuna, D. H. Fair-  
 677 field, J. A. Slavin, W. Riedler, K. Schwingenschuh, and M. G. Kivelson (1997),  
 678 The Cluster Magnetic Field Investigation, *Space Science Reviews*, **79**, 65–91, doi:  
 679 10.1023/A:1004970907748.
- 680 Balogh, A., C. M. Carr, M. H. Acuña, M. W. Dunlop, T. J. Beek, P. Brown,  
 681 K. Fornacon, E. Georgescu, K. Glassmeier, J. Harris, G. Musmann, T. Oddy, and  
 682 K. Schwingenschuh (2001), The Cluster Magnetic Field Investigation: overview of  
 683 in-flight performance and initial results, *Annales Geophysicae*, **19**, 1207–1217.
- 684 Bartels, J., N. H. Heck, and H. F. Johnston (1939), The three-hour-range index mea-  
 685 suring geomagnetic activity, *Terrestrial Magnetism and Atmospheric Electricity*  
 686 (*Journal of Geophysical Research*), **44**, 411, doi:10.1029/TE044i004p00411.
- 687 Blagau, A., I. Dandouras, A. Barthe, S. Brunato, G. Facskó, and V. Constanti-  
 688 nescu (2013), In-flight calibration of Hot Ion Analyser onboard Cluster, *Geo-  
 689 scientific Instrumentation, Methods and Data Systems Discussions*, **3**, 407–435,  
 690 doi:10.5194/gid-3-407-2013.
- 691 Blagau, A., I. Dandouras, A. Barthe, S. Brunato, G. Facskó, and V. Constantinescu  
 692 (2014), In-flight calibration of the Hot Ion Analyser on board Cluster, *Geoscientific  
 693 Instrumentation, Methods and Data Systems*, **3**, 49–58, doi:10.5194/gi-3-49-

- 694 2014.
- 695 Chittenden, J. P., S. V. Lebedev, C. A. Jennings, S. N. Bland , and A. Ciardi  
 696 (2004), X-ray generation mechanisms in three-dimensional simulations of wire  
 697 array Z-pinches, *Plasma Physics and Controlled Fusion*, *46*(12B), B457–B476,  
 698 doi:10.1088/0741-3335/46/12B/039.
- 699 Ciardi, A., S. V. Lebedev, A. Frank, E. G. Blackman, J. P. Chittenden, C. J. Jen-  
 700 nings, D. J. Ampleford, S. N. Bland, S. C. Bott, J. Rapley, G. N. Hall, F. A.  
 701 Suzuki-Vidal, A. Marocchino, T. Lery, and C. Stehle (2007), The evolution of  
 702 magnetic tower jets in the laboratory, *Physics of Plasmas*, *14*(5), 056,501–056,501,  
 703 doi:10.1063/1.2436479.
- 704 Credland, J., G. Mecke, and J. Ellwood (1997), The Cluster Mission: ESA‘S  
 705 Spacefleet to the Magnetosphere, *Space Science Reviews*, *79*, 33–64, doi:  
 706 10.1023/A:1004914822769.
- 707 Davis, T. N., and M. Sugiura (1966), Auroral electrojet activity index AE and its  
 708 universal time variations, *Journal of Geophysical Research*, *71*, 785–801, doi:  
 709 10.1029/JZ071i003p00785.
- 710 Décréau, P. M. E., P. Fergeau, V. Krasnoselskikh, E. Le Guiriec, M. Lévêque,  
 711 P. Martin, O. Randriamboarison, J. L. Rauch, F. X. Sené, H. C. Séran, J. G.  
 712 Trotignon, P. Canu, N. Cornilleau, H. de Féraudy, H. Alleyne, K. Yearby, P. B.  
 713 Mögensen, G. Gustafsson, M. André, D. C. Gurnett, F. Darrouzet, J. Lemaire,  
 714 C. C. Harvey, P. Travnicek, and Whisper Experimenters Group (2001), Early re-  
 715 sults from the Whisper instrument on Cluster: an overview, *Annales Geophysicae*,  
 716 *19*, 1241–1258, doi:10.5194/angeo-19-1241-2001.
- 717 Escoubet, C. P., M. Fehringer, and M. Goldstein (2001), Introduction The Cluster  
 718 mission, *Annales Geophysicae*, *19*, 1197–1200, doi:10.5194/angeo-19-1197-2001.
- 719 Facskó, G., I. Honkonen, T. Živković, L. Palin, E. Kallio, K. Ågren, H. Opgenoorth,  
 720 E. I. Tanskanen, and S. Milan (2016), One year in the Earth’s magnetosphere: A  
 721 global MHD simulation and spacecraft measurements, *Space Weather*, *14*, 351–  
 722 367, doi:10.1002/2015SW001355.
- 723 Facskó, G., T. B. Balogh, E. I. Anekallu, C. R. and Tanskanen, P. Peitso, L. Degener,  
 724 M. Kangwa, T. Laitinen, and S. Laakso, H. Burley (in preparation), Bow shock  
 725 identification in cluster measurements, *Space Weather*.
- 726 Fazakerley, A. N., A. D. Lahiff, R. J. Wilson, I. Rozum, C. Anekallu, M. West, and

- 727 H. Bacai (2010a), PEACE Data in the Cluster Active Archive, *Astrophysics and*  
728 *Space Science Proceedings*, 11, 129–144, doi:10.1007/978-90-481-3499-1\_8.
- 729 Fazakerley, A. N., A. D. Lahiff, I. Rozum, D. Kataria, H. Bacai, C. Anekallu,  
730 M. West, and A. Åsnes (2010b), Cluster-PEACE In-flight Calibration Status,  
731 *Astrophysics and Space Science Proceedings*, 11, 281–299, doi:10.1007/978-90-481-  
732 3499-1\_19.
- 733 García, K. S., and W. J. Hughes (2007), Finding the Lyon-Fedder-Mobarry mag-  
734 netopause: A statistical perspective, *Journal of Geophysical Research (Space*  
735 *Physics)*, 112(A6), A06229, doi:10.1029/2006JA012039.
- 736 Gordeev, E., G. Facskó, V. Sergeev, I. Honkonen, M. Palmroth, P. Janhunen, and  
737 S. Milan (2013), Verification of the GUMICS-4 global MHD code using empirical  
738 relationships, *Journal of Geophysical Research (Space Physics)*, 118, 3138–3146,  
739 doi:10.1002/jgra.50359.
- 740 Greenwald, R. A., K. B. Baker, J. R. Dudeney, M. Pinnock, T. B. Jones, E. C.  
741 Thomas, J.-P. Villain, J.-C. Cerisier, C. Senior, C. Hanuise, R. D. Hunsucker,  
742 G. Sofko, J. Koehler, E. Nielsen, R. Pellinen, A. D. M. Walker, N. Sato,  
743 and H. Yamagishi (1995), Darn/Superdarn: A Global View of the Dynam-  
744 ics of High-Latitude Convection, *Space Science Reviews*, 71, 761–796, doi:  
745 10.1007/BF00751350.
- 746 Guild, T. B., H. E. Spence, E. L. Kepko, V. Merkin, J. G. Lyon, M. Wiltberger, and  
747 C. C. Goodrich (2008a), Geotail and LFM comparisons of plasma sheet clima-  
748 tology: 1. Average values, *Journal of Geophysical Research (Space Physics)*, 113,  
749 A04216, doi:10.1029/2007JA012611.
- 750 Guild, T. B., H. E. Spence, E. L. Kepko, V. Merkin, J. G. Lyon, M. Wiltberger, and  
751 C. C. Goodrich (2008b), Geotail and LFM comparisons of plasma sheet climatol-  
752 ogy: 2. Flow variability, *Journal of Geophysical Research (Space Physics)*, 113,  
753 A04217, doi:10.1029/2007JA012613.
- 754 Gustafsson, G., R. Bostrom, B. Holback, G. Holmgren, A. Lundgren, K. Stasiewicz,  
755 L. Ahlen, F. S. Mozer, D. Pankow, P. Harvey, P. Berg, R. Ulrich, A. Pedersen,  
756 R. Schmidt, A. Butler, A. W. C. Fransen, D. Klinge, M. Thomsen, C.-G. Faltham-  
757 mar, P.-A. Lindqvist, S. Christenson, J. Holtet, B. Lybekk, T. A. Sten, P. Tan-  
758 skanen, K. Lappalainen, and J. Wygant (1997), The Electric Field and Wave  
759 Experiment for the Cluster Mission, *Space Science Reviews*, 79, 137–156, doi:

- 760 10.1023/A:1004975108657.
- 761 Gustafsson, G., M. André, T. Carozzi, A. I. Eriksson, C.-G. Fälthammar, R. Grard,  
762 G. Holmgren, J. A. Holtet, N. Ivchenko, T. Karlsson, Y. Khotyaintsev, S. Klimov,  
763 H. Laakso, P.-A. Lindqvist, B. Lybekk, G. Marklund, F. Mozer, K. Mursula,  
764 A. Pedersen, B. Popielawska, S. Savin, K. Stasiewicz, P. Tanskanen, A. Vaivads,  
765 and J.-E. Wahlund (2001), First results of electric field and density observations  
766 by Cluster EFW based on initial months of operation, *Annales Geophysicae*, 19,  
767 1219–1240, doi:10.5194/angeo-19-1219-2001.
- 768 Haiducek, J. D., D. T. Welling, N. Y. Ganushkina, S. K. Morley, and D. S. Oz-  
769 turk (2017), SWMF Global Magnetosphere Simulations of January 2005: Geo-  
770 magnetic Indices and Cross-Polar Cap Potential, *Space Weather*, 15, 1567–1587,  
771 doi:10.1002/2017SW001695.
- 772 Iyemori, T. (1990), Storm-time magnetospheric currents inferred from mid-latitude  
773 geomagnetic field variations, *Journal of Geomagnetism and Geoelectricity*, 42,  
774 1249–1265, doi:10.5636/jgg.42.1249.
- 775 Janhunen, P., M. Palmroth, T. Laitinen, I. Honkonen, L. Juusola, G. Facskó, and  
776 T. I. Pulkkinen (2012), The GUMICS-4 global MHD magnetosphere-ionosphere  
777 coupling simulation, *Journal of Atmospheric and Solar-Terrestrial Physics*, 80,  
778 48–59, doi:10.1016/j.jastp.2012.03.006.
- 779 Johnstone, A. D., C. Alsop, S. Burge, P. J. Carter, A. J. Coates, A. J. Coker, A. N.  
780 Fazakerley, M. Grande, R. A. Gowen, C. Gurgiolo, B. K. Hancock, B. Narheim,  
781 A. Preece, P. H. Sheather, J. D. Winningham, and R. D. Woodliffe (1997), Peace:  
782 a Plasma Electron and Current Experiment, *Space Science Reviews*, 79, 351–398,  
783 doi:10.1023/A:1004938001388.
- 784 Juusola, L., O. Amm, K. Kauristie, and A. Viljanen (2007), A model for estimating  
785 the relation between the Hall to Pedersen conductance ratio and ground magnetic  
786 data derived from CHAMP satellite statistics, *Annales Geophysicae*, 25, 721–736,  
787 doi:10.5194/angeo-25-721-2007.
- 788 Juusola, L., G. Facskó, I. Honkonen, P. Janhunen, H. Vanhamäki, K. Kauristie,  
789 T. V. Laitinen, S. E. Milan, M. Palmroth, E. I. Tanskanen, and A. Viljanen  
790 (2014), Statistical comparison of seasonal variations in the GUMICS-4 global  
791 MHD model ionosphere and measurements, *Space Weather*, 12, 582–600, doi:  
792 10.1002/2014SW001082.

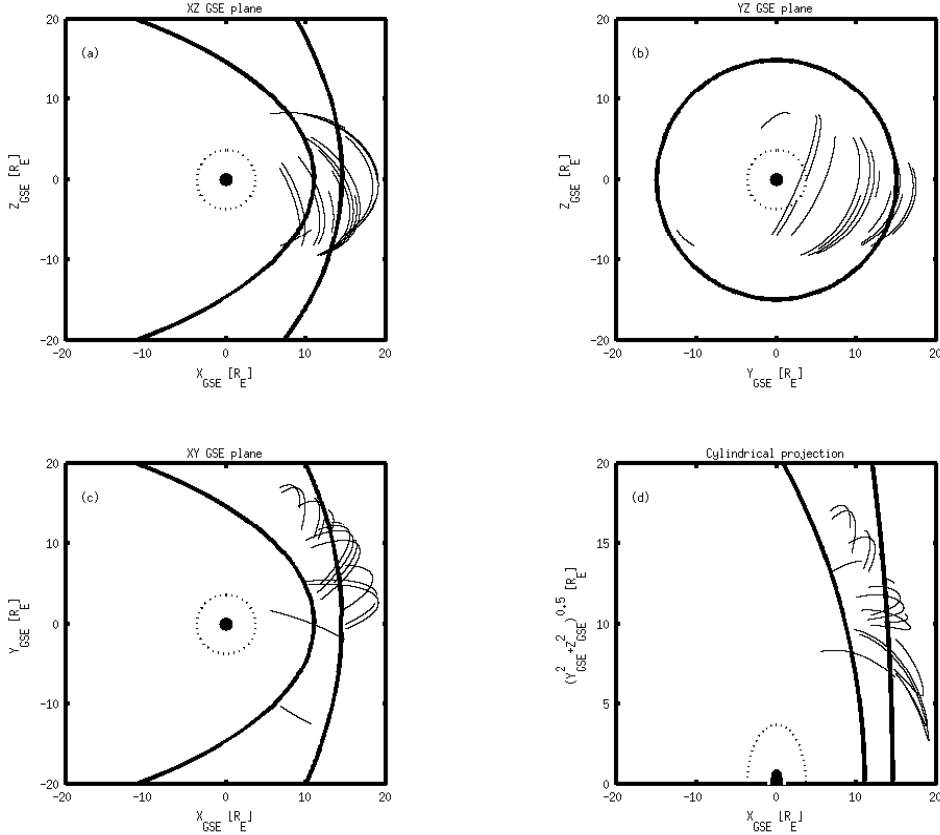
- 793 Kallio, E., and G. Facskó (2015), Properties of plasma near the moon in the magne-  
794 totail, *Planetary and Space Science*, *115*, 69–76, doi:10.1016/j.pss.2014.11.007.
- 795 Kokubun, S., T. Yamamoto, M. H. Acuña, K. Hayashi, K. Shiokawa, and H. Kawano  
796 (1994), The GEOTAIL Magnetic Field Experiment., *Journal of Geomagnetism*  
797 and *Geoelectricity*, *46*, 7–21, doi:10.5636/jgg.46.7.
- 798 Lakka, A., T. I. Pulkkinen, A. P. Dimmock, M. Myllys, I. Honkonen, and M. Palm-  
799 roth (2018a), The Cross-Polar Cap Saturation in GUMICS-4 During High Solar  
800 Wind Driving, *Journal of Geophysical Research (Space Physics)*, *123*, 3320–3332,  
801 doi:10.1002/2017JA025054.
- 802 Lakka, A., T. I. Pulkkinen, A. P. Dimmock, E. Kilpuu, M. Ala-Lahti, I. Honko-  
803 nen, M. Palmroth, and Raukunen (2018b), Icme impact at earth with low and  
804 typical mach number plasma characteristics, *Annales Geophysicae Discussions*,  
805 <https://doi.org/10.5194/angeo-2018-81>.
- 806 Lani, A., A. Sanna, N. Villedieu, and M. Panesi (2012), COOLFluiD an Open Com-  
807 putational Platform for Aerothermodynamics and Flow-Radiation Coupling, in  
808 *ESA Special Publication, ESA Special Publication*, vol. 714, p. 45.
- 809 Liemohn, M., N. Y. Ganushkina, D. L. De Zeeuw, L. Rastaetter, M. Kuznetsova,  
810 D. T. Welling, G. Toth, R. Ilie, T. I. Gombosi, and B. van der Holst (2018), Real-  
811 Time SWMF at CCMC: Assessing the Dst Output From Continuous Operational  
812 Simulations, *Space Weather*, *16*(10), 1583–1603, doi:10.1029/2018SW001953.
- 813 Lyon, J. G., J. A. Fedder, and C. M. Mobarry (2004), The Lyon-Fedder-Mobarry  
814 (LFM) global MHD magnetospheric simulation code, *Journal of Atmospheric and*  
815 *Solar-Terrestrial Physics*, *66*, 1333–1350, doi:10.1016/j.jastp.2004.03.020.
- 816 Mejnertsen, L., J. P. Eastwood, J. P. Chittenden, and A. Masters (2016), Global  
817 MHD simulations of Neptune’s magnetosphere, *Journal of Geophysical Research*  
818 (*Space Physics*), *121*(8), 7497–7513, doi:10.1002/2015JA022272.
- 819 Mejnertsen, L., J. P. Eastwood, H. Hietala, S. J. Schwartz, and J. P. Chittenden  
820 (2018), Global MHD Simulations of the Earth’s Bow Shock Shape and Motion  
821 Under Variable Solar Wind Conditions, *Journal of Geophysical Research (Space*  
822 *Physics*), *123*(1), 259–271, doi:10.1002/2017JA024690.
- 823 Mukai, T., S. Machida, Y. Saito, M. Hirahara, T. Terasawa, N. Kaya, T. Obara,  
824 M. Ejiri, and A. Nishida (1994), The Low Energy Particle (LEP) Experiment on-  
825 board the GEOTAIL Satellite., *Journal of Geomagnetism and Geoelectricity*, *46*,

- 826 669–692, doi:10.5636/jgg.46.669.
- 827 Peredo, M., J. A. Slavin, E. Mazur, and S. A. Curtis (1995), Three-dimensional po-  
828 sition and shape of the bow shock and their variation with Alfvénic, sonic and  
829 magnetosonic Mach numbers and interplanetary magnetic field orientation, *Jour-*  
830 *nal of Geophysical Research*, 100, 7907–7916, doi:10.1029/94JA02545.
- 831 Poedts, S., A. Kochanov, A. Lani, C. Scolini, C. Verbeke, S. Hosteaux, E. Chané,  
832 H. Deconinck, N. Mihalache, F. Diet, D. Heynderickx, J. De Keyser, E. De  
833 Donder, N. B. Crosby, M. Echim, L. Rodriguez, R. Vansintjan, F. Verstringe,  
834 B. Mampaey, R. Horne, S. Glauert, P. Jiggens, R. Keil, A. Glover, G. Deprez, and  
835 J.-P. Luntama (2020), The Virtual Space Weather Modelling Centre, *Journal of*  
836 *Space Weather and Space Climate*, 10, 14, doi:10.1051/swsc/2020012.
- 837 Powell, K. G., P. L. Roe, T. J. Linde, T. I. Gombosi, and D. L. De Zeeuw (1999), A  
838 Solution-Adaptive Upwind Scheme for Ideal Magnetohydrodynamics, *Journal of*  
839 *Computational Physics*, 154, 284–309, doi:10.1006/jcph.1999.6299.
- 840 Raeder, J., D. Larson, W. Li, E. L. Kepko, and T. Fuller-Rowell (2008), OpenG-  
841 GCM Simulations for the THEMIS Mission, *Space Science Reviews*, 141, 535–555,  
842 doi:10.1007/s11214-008-9421-5.
- 843 Reigber, C., H. Lühr, and P. Schwintzer (2002), CHAMP mission status, *Advances*  
844 *in Space Research*, 30, 129–134, doi:10.1016/S0273-1177(02)00276-4.
- 845 Rème, H., J. M. Bosqued, J. A. Sauvaud, A. Cros, J. Dandouras, C. Aoustin,  
846 J. Bouyssou, T. Camus, J. Cuvilo, C. Martz, J. L. Medale, H. Perrier, D. Rome-  
847 fort, J. Rouzaud, C. D'Uston, E. Möbius, K. Crocker, M. Granoff, L. M. Kistler,  
848 M. Popecki, D. Hovestadt, B. Klecker, G. Paschmann, M. Scholer, C. W. Carl-  
849 son, D. W. Curtis, R. P. Lin, J. P. McFadden, V. Formisano, E. Amata, M. B.  
850 Bavassano-Cattaneo, P. Baldetti, G. Bellucci, R. Bruno, G. Chionchio, A. di Lel-  
851 lis, E. G. Shelley, A. G. Ghielmetti, W. Lennartsson, A. Korth, H. Rosenbauer,  
852 R. Lundin, S. Olsen, G. K. Parks, M. McCarthy, and H. Balsiger (1997), The  
853 Cluster Ion Spectrometry (CIS) Experiment, *Space Science Reviews*, 79, 303–350,  
854 doi:10.1023/A:1004929816409.
- 855 Rème, H., C. Aoustin, J. M. Bosqued, I. Dandouras, B. Lavraud, J. A. Sauvaud,  
856 A. Barthe, J. Bouyssou, T. Camus, O. Coeur-Joly, A. Cros, J. Cuvilo, F. Ducay,  
857 Y. Garbarowitz, J. L. Medale, E. Penou, H. Perrier, D. Romefort, J. Rouzaud,  
858 C. Vallat, D. Alcaydé, C. Jacquay, C. Mazelle, C. D'Uston, E. Möbius, L. M.

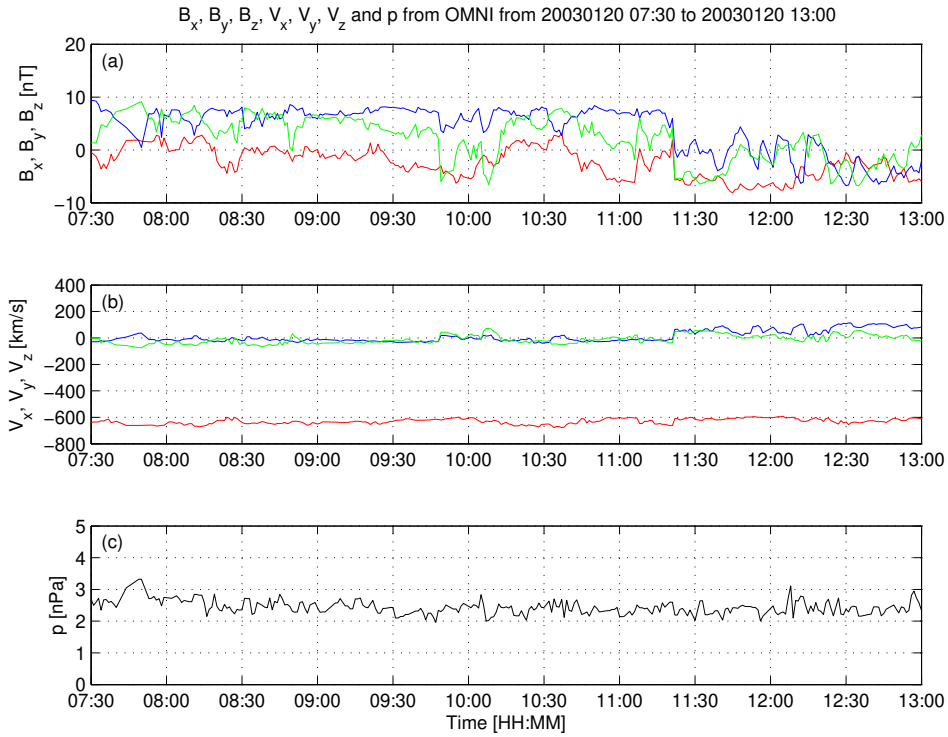
- 859 Kistler, K. Crocker, M. Granoff, C. Mouikis, M. Popecki, M. Vosbury, B. Klecker,  
 860 D. Hovestadt, H. Kucharek, E. Kuenneth, G. Paschmann, M. Scholer, N. Sckopke,  
 861 E. Seidenschwang, C. W. Carlson, D. W. Curtis, C. Ingraham, R. P. Lin, J. P.  
 862 McFadden, G. K. Parks, T. Phan, V. Formisano, E. Amata, M. B. Bavassano-  
 863 Cattaneo, P. Baldetti, R. Bruno, G. Chionchio, A. di Lellis, M. F. Marcucci,  
 864 G. Pallocchia, A. Korth, P. W. Daly, B. Graeve, H. Rosenbauer, V. Vasylunas,  
 865 M. McCarthy, M. Wilber, L. Eliasson, R. Lundin, S. Olsen, E. G. Shelley, S. Fuse-  
 866 lier, A. G. Ghielmetti, W. Lennartsson, C. P. Escoubet, H. Balsiger, R. Friedel, J.-  
 867 B. Cao, R. A. Kovrashkin, I. Papamastorakis, R. Pellat, J. Scudder, and B. Son-  
 868 nerup (2001), First multispacecraft ion measurements in and near the Earth's  
 869 magnetosphere with the identical Cluster ion spectrometry (CIS) experiment,  
 870 *Annales Geophysicae*, *19*, 1303–1354, doi:10.5194/angeo-19-1303-2001.
- 871 Ritter, P., H. Lühr, A. Viljanen, O. Amm, A. Pulkkinen, and I. Sillanpää (2004),  
 872 Ionospheric currents estimated simultaneously from CHAMP satellite and IMAGE  
 873 ground-based magnetic field measurements: a statistical study at auroral latitudes,  
 874 *Annales Geophysicae*, *22*, 417–430, doi:10.5194/angeo-22-417-2004.
- 875 Rostoker, G. (1972), Geomagnetic indices., *Reviews of Geophysics and Space  
 876 Physics*, *10*, 935–950, doi:10.1029/RG010i004p00935.
- 877 Siscoe, G. L., G. M. Erickson, B. U. Sonnerup, N. C. Maynard, J. A. Schoendorf,  
 878 K. D. Siebert, D. R. Weimer, W. W. White, and G. R. Wilson (2001), The Mag-  
 879 netospheric Fluopause, in *AGU Spring Meeting Abstracts*, vol. 2001, pp. SM52D–  
 880 02.
- 881 Sofko, G. J., R. Greenwald, and W. Bristow (1995), Direct determination of large-  
 882 scale magnetospheric field-aligned currents with SuperDARN, *Geophysical Re-  
 883 search Letters*, *22*, 2041–2044, doi:10.1029/95GL01317.
- 884 Thomsen, M. F. (2004), Why  $K_p$  is such a good measure of magnetospheric convec-  
 885 tion, *Space Weather*, *2*, S11004, doi:10.1029/2004SW000089.
- 886 Tóth, G., I. V. Sokolov, T. I. Gombosi, D. R. Chesney, C. R. Clauer, D. L. de  
 887 Zeeuw, K. C. Hansen, K. J. Kane, W. B. Manchester, R. C. Oehmke, K. G. Pow-  
 888 ell, A. J. Ridley, I. I. Roussev, Q. F. Stout, O. Volberg, R. A. Wolf, S. Sazykin,  
 889 A. Chan, B. Yu, and J. Kóta (2005), Space Weather Modeling Framework: A  
 890 new tool for the space science community, *Journal of Geophysical Research (Space  
 891 Physics)*, *110*, A12226, doi:10.1029/2005JA011126.

- 892 Tóth, G., B. van der Holst, I. V. Sokolov, D. L. De Zeeuw, T. I. Gombosi, F. Fang,  
893 W. B. Manchester, X. Meng, D. Najib, K. G. Powell, Q. F. Stout, A. Glo-  
894 cer, Y.-J. Ma, and M. Opher (2012), Adaptive numerical algorithms in space  
895 weather modeling, *Journal of Computational Physics*, 231, 870–903, doi:  
896 10.1016/j.jcp.2011.02.006.
- 897 Trotignon, J. G., P. M. E. Décréau, J. L. Rauch, X. Vallières, A. Rochel,  
898 S. Kouglénou, G. Lointier, G. Facskó, P. Canu, F. Darrouzet, and A. Masson  
899 (2010), The WHISPER Relaxation Sounder and the CLUSTER Active Archive,  
900 *Astrophysics and Space Science Proceedings*, 11, 185–208, doi:10.1007/978-90-481-  
901 3499-1\_12.
- 902 Trotignon, J.-G., Vallières, and the WHISPER team (2011), Calibration report of  
903 the whisper measurements in the cluster active archive (caa), *Tech. rep.*, LPC2E  
904 CNRS, caa-est-cr-whi.
- 905 Tsyganenko, N. A. (1995), Modeling the Earth's magnetospheric magnetic field  
906 confined within a realistic magnetopause, *Journal of Geophysical Research*, 100,  
907 5599–5612, doi:10.1029/94JA03193.
- 908 Vörös, Z., G. Facskó, M. Khodachenko, I. Honkonen, P. Janhunen, and M. Palmroth  
909 (2014), Windsock memory COnditioned RAM (CO-RAM) pressure effect: Forced  
910 reconnection in the Earth's magnetotail, *Journal of Geophysical Research (Space  
911 Physics)*, 119, 6273–6293, doi:10.1002/2014JA019857.
- 912 Wang, Z.-D., and R. L. Xu (1994), Signatures of the magnetotail neutral sheet,  
913 *Geophysical Research Letters*, 21(19), 2087–2090, doi:10.1029/94GL01960.
- 914 Weimer, D. R. (2005), Improved ionospheric electrodynamic models and applica-  
915 tion to calculating Joule heating rates, *Journal of Geophysical Research (Space  
916 Physics)*, 110, A05306, doi:10.1029/2004JA010884.
- 917 Wiltberger, M., E. J. Rigler, V. Merkin, and J. G. Lyon (2017), Structure of High  
918 Latitude Currents in Magnetosphere-Ionosphere Models, *Space Science Reviews*,  
919 206, 575–598, doi:10.1007/s11214-016-0271-2.
- 920 Zhang, B., W. Lotko, M. J. Wiltberger, O. J. Brambles, and P. A. Damiano (2011),  
921 A statistical study of magnetosphere-ionosphere coupling in the Lyon-Fedder-  
922 Mobarry global MHD model, *Journal of Atmospheric and Solar-Terrestrial  
923 Physics*, 73, 686–702, doi:10.1016/j.jastp.2010.09.027.
- 924 Zhang, B., K. A. Sorathia, J. G. Lyon, V. G. Merkin, J. S. Garretson, and M. Wilt-

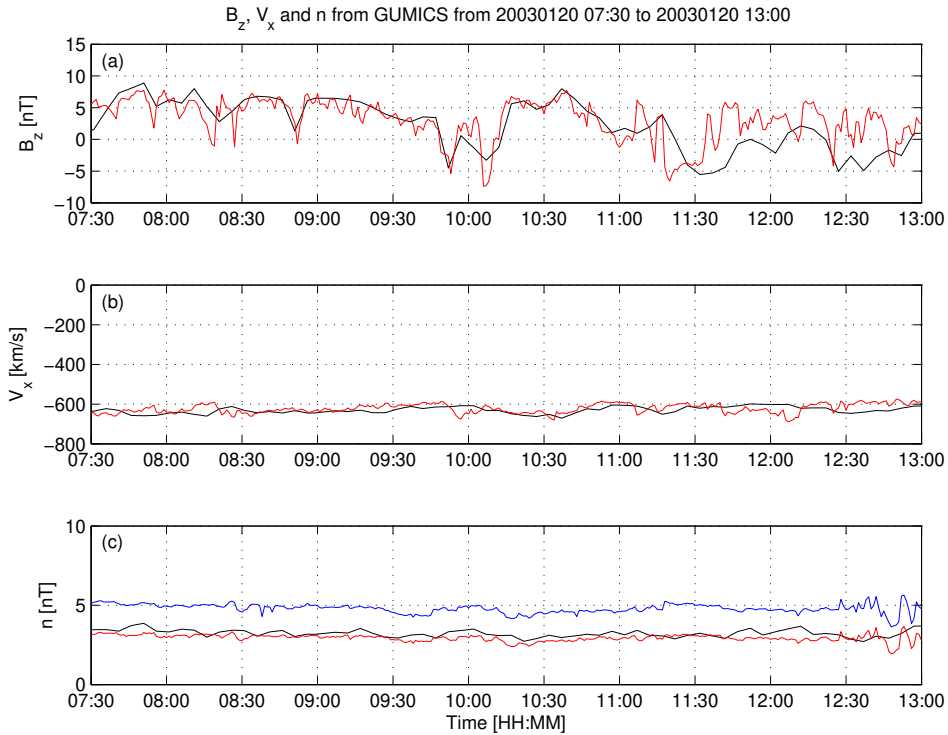
925 berger (2019), GAMERA: A Three-dimensional Finite-volume MHD Solver for  
926 Non-orthogonal Curvilinear Geometries, *The Astrophysical Journal Supplement*  
927 *Series*, 244(1), 20, doi:10.3847/1538-4365/ab3a4c.



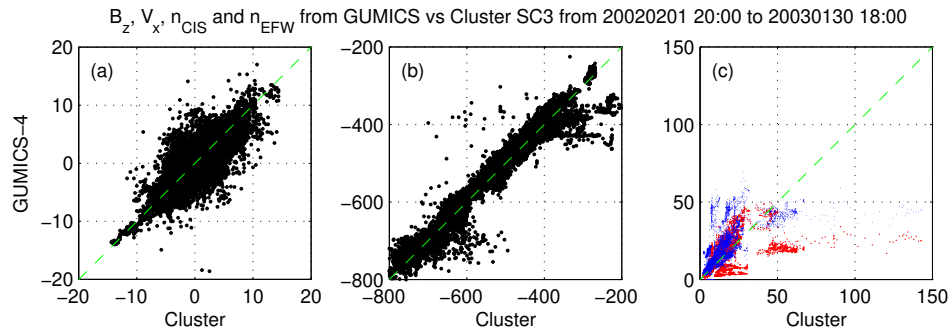
928 **Figure 1.** Cluster SC3 orbit in the solar wind in GSE system for all intervals (see Table 1).  
929 (a) XZ (b) YZ (c) XY (d) Cylindrical projection. Average bow-shock and magnetopause po-  
930 sitions are drawn on all plots using **thick** solid lines [Perego *et al.*, 1995; Tsyganenko, 1995,  
931 respectively]. The black dots at  $3.7 R_E$  show the boundary of the GUMICS-4 inner magneto-  
932 spheric domain. The black circle in the origo of all plots shows the size of the Earth.



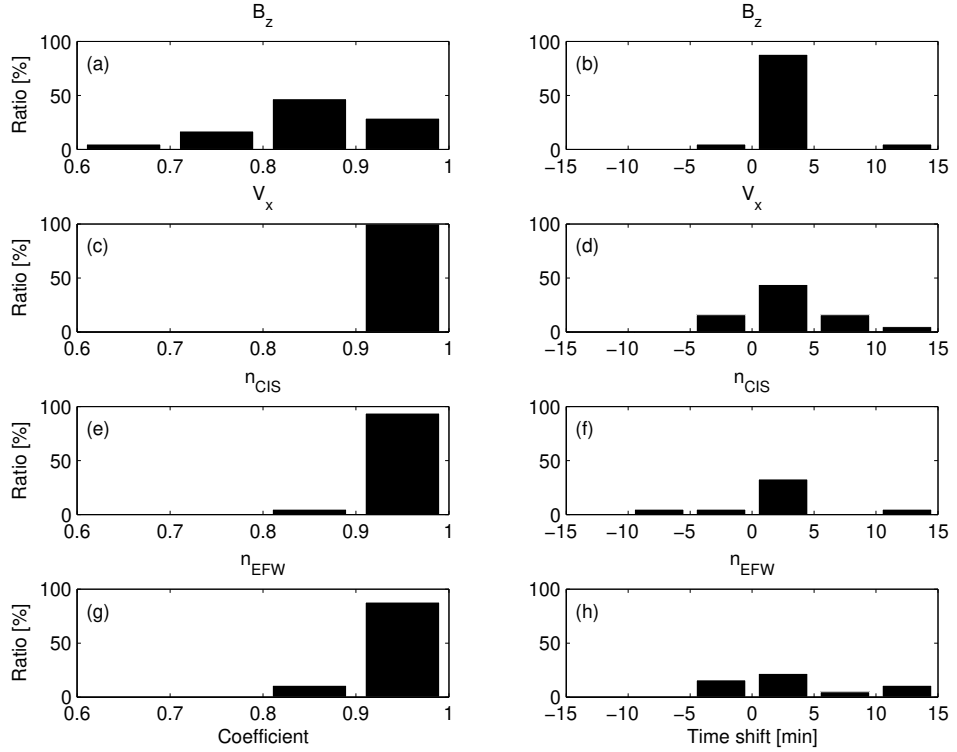
933 **Figure 2.** OMNI solar wind data in GSE system from 7:30 to 13:00 (UT) on January 20,  
 934 2003. (a) Magnetic field  $B_x$  (red),  $B_y$  (green) and  $B_z$  (blue) components. (b) Solar wind velocity  
 935  $V_x$  (red),  $V_y$  (green) and  $V_z$  (blue) components. (c) The  $P$  pressure of the solar wind (black).



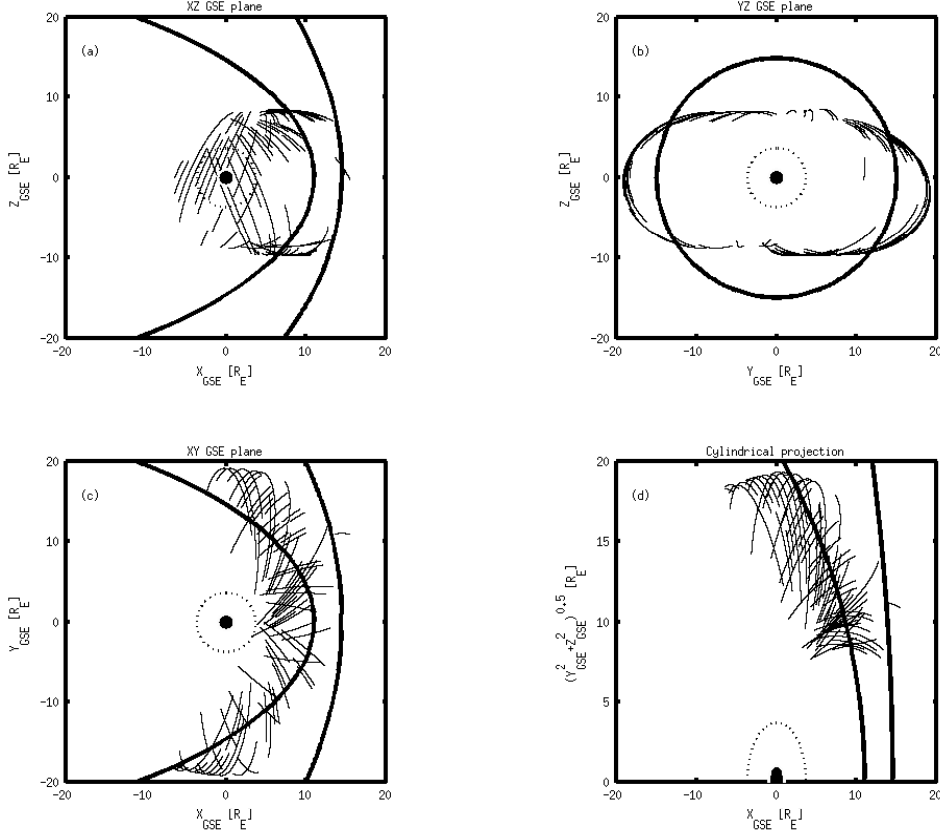
936      **Figure 3.** GUMICS-4 simulation results (black) and Cluster SC3 magnetic field Z component,  
 937      ion plasma moments (red) and electron density calculated from spacecraft potential (blue) from  
 938      January 20, 2003 from 7:30 to 13:00 (UT) in the solar wind in GSE system. (a) Magnetic field Z  
 939      component. (b) Solar wind velocity X component (c) Solar wind density.



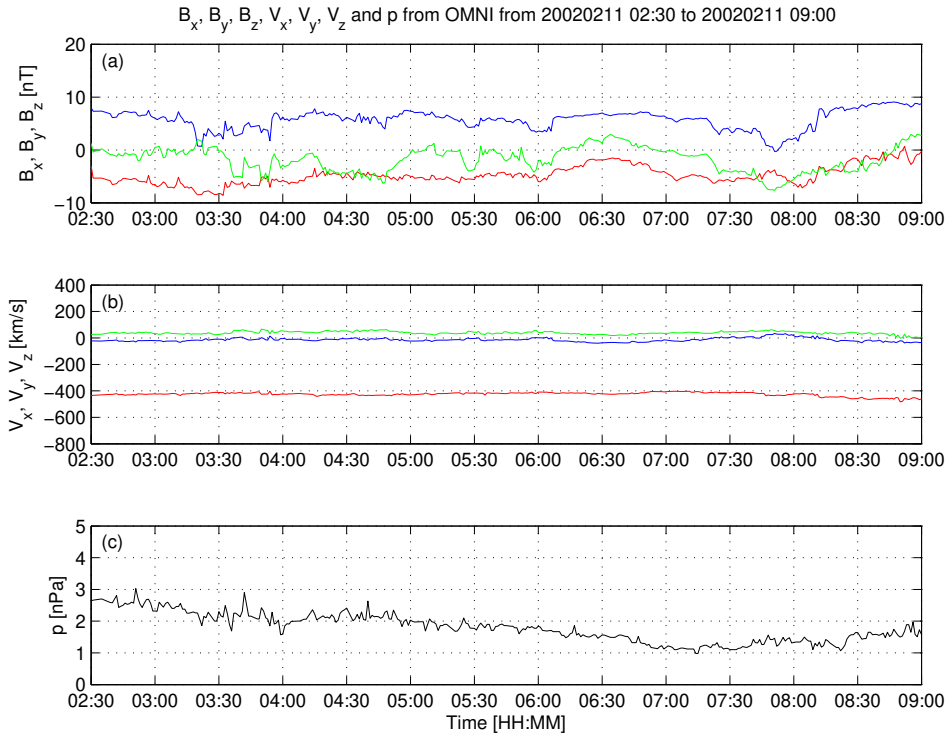
940 **Figure 4.** Scattered plots of the Cluster SC3 and GUMICS-4 simulations for all intervals in  
 941 the solar wind. The dashed line is the  $y=x$  line. (a) Magnetic field Z component in GSE system.  
 942 (b) Solar wind velocity X component in GSE system. (c) Solar wind density measured by the  
 943 CIS HIA instrument (red) and calculated from the spacecraft potential (blue).



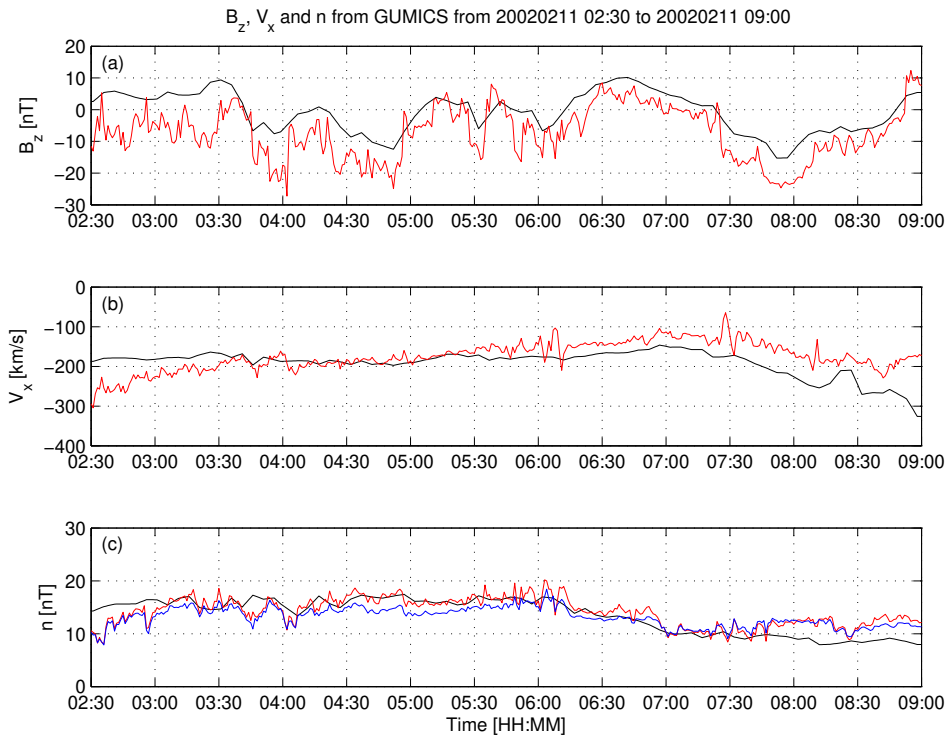
944      **Figure 5.** The distributions of the **highest** correlation coefficients (a, c, e, g) of the magnetic  
 945      field Z component ( $B_z$ ) in GSE system, solar wind velocity X component ( $V_x$ ) in GSE system,  
 946      the solar wind density measured by the CIS HIA ( $n_{CIS}$ ) instrument and calculated from the  
 947      spacecraft potential ( $n_{EFW}$ ), respectively, for all intervals in the solar wind. The distributions of  
 948      the **corresponding** time shifts (b, d, f, h) of the  $B_z$ , the  $V_x$ , the  $n_{CIS}$  and the  $n_{EFW}$ ), respec-  
 949      tively, for all intervals in the solar wind.



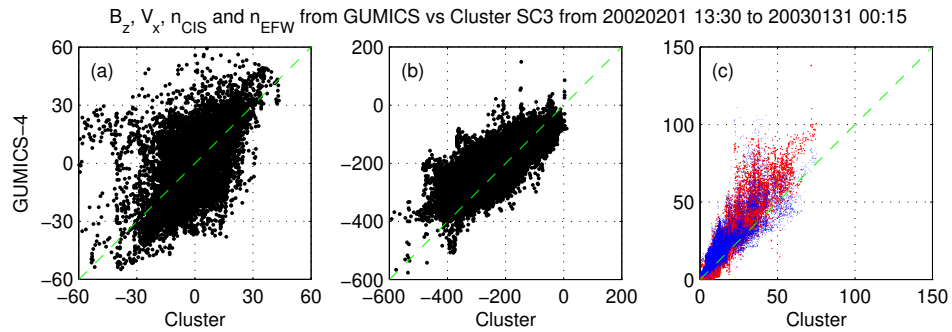
950      **Figure 6.** Cluster SC3 orbit in the magnetosheath in GSE system for all intervals (see Ta-  
 951      ble 2). (a) XZ (b) YZ (c) XY (d) Cylindrical projection. Average bow-shock and magnetopause  
 952      positions are drawn on all plots using **thick** solid lines [Peredo *et al.*, 1995; Tsyganenko, 1995,  
 953      respectively]. The black dots at  $3.7 R_E$  show the boundary of the GUMICS-4 inner magneto-  
 954      spheric domain. The black circle in the origo of all plots shows the size of the Earth.



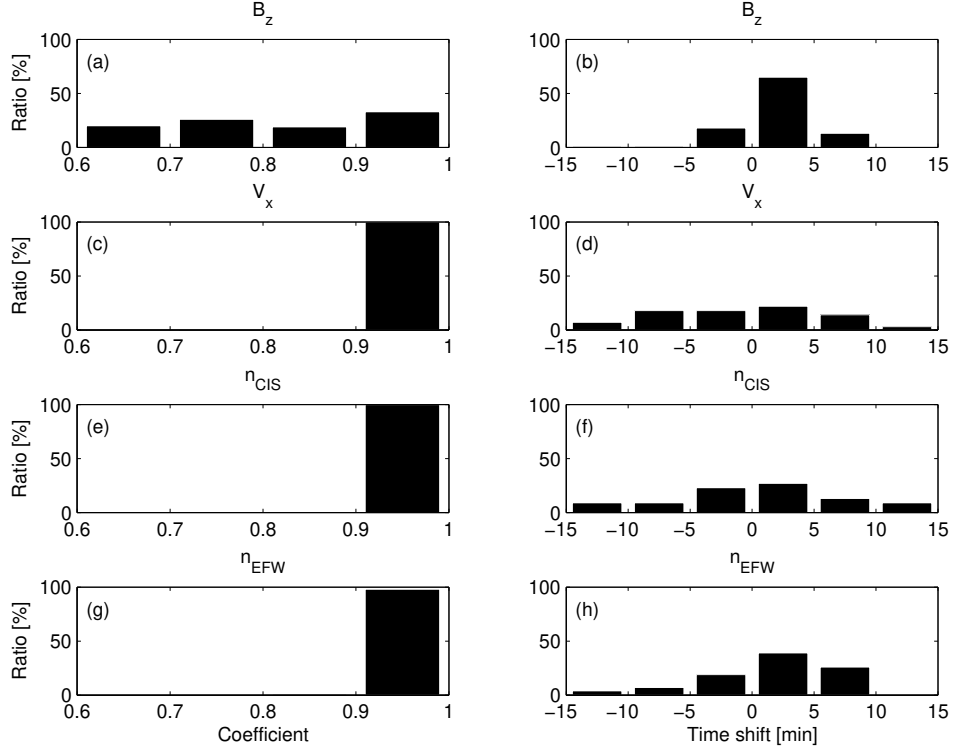
955      **Figure 7.** OMNI solar wind data in GSE system from 2:30 to 09:00 (UT) on February 11,  
956      2002. (a) Magnetic field  $B_x$  (red),  $B_y$  (green) and  $B_z$  (blue) components. (b) Solar wind velocity  
957       $V_x$  (red),  $V_y$  (green) and  $V_z$  (blue) components. (c) The  $P$  pressure of the solar wind (black).



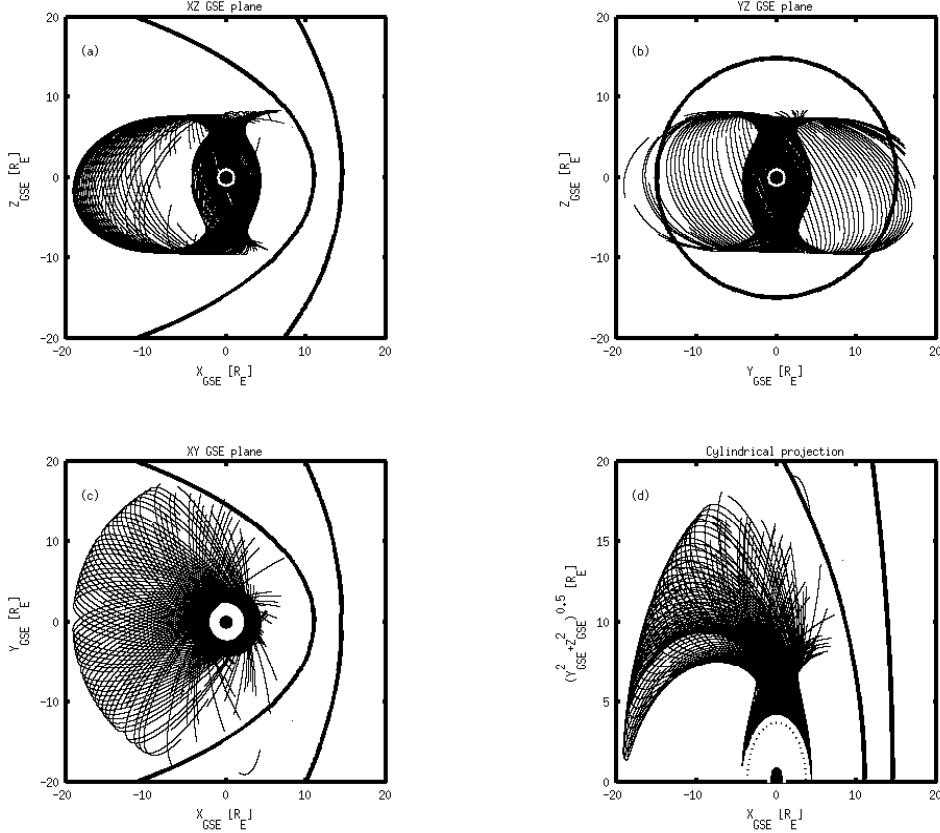
958      **Figure 8.** GUMICS-4 simulation results (black) and Cluster SC3 magnetic field Z component,  
 959      ion plasma moments (red) and electron density calculated from spacecraft potential (blue) from  
 960      February 11, 2002 from 2:30 to 9:00 (UT) in the magnetosheath in GSE system (a) Magnetic  
 961      field Z component. (b) Solar wind velocity X component (c) Solar wind density.



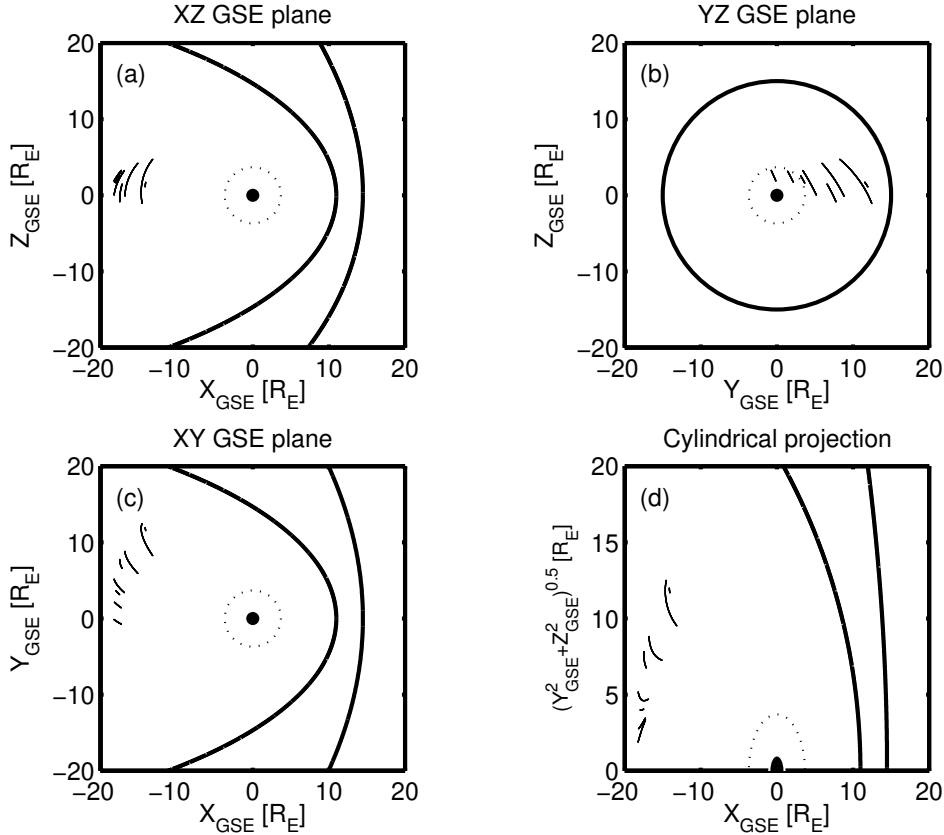
962 **Figure 9.** Scattered plots of the Cluster SC3 and GUMICS-4 simulations for all intervals in  
 963 the magnetosheath in GSE system. The dashed line is the  $y=x$  line. (a) Magnetic field Z com-  
 964 ponent. (b) Solar wind velocity X component. (c) Solar wind density measured by the CIS HIA  
 965 instrument (red) and calculated from the spacecraft potential (blue).



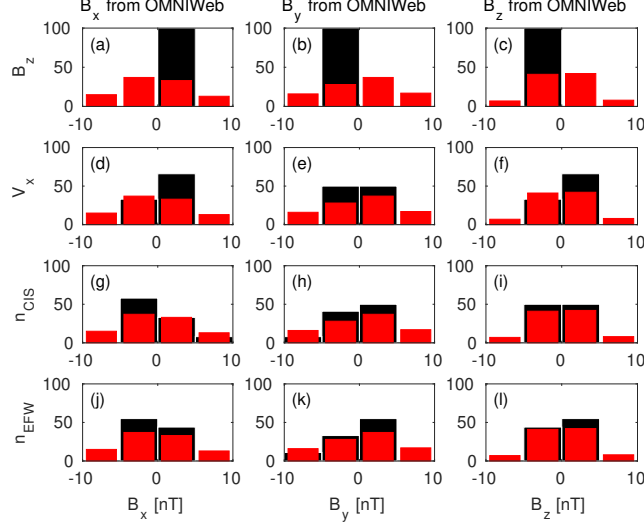
966      **Figure 10.** The distributions of the correlation coefficients (a, c, e, g) of the magnetic field Z  
 967      component ( $B_z$ ) in GSE system, solar wind velocity X component ( $V_X$ ) in GSE system, the solar  
 968      wind density measured by the CIS HIA ( $n_{CIS}$ ) instrument and calculated from the spacecraft  
 969      potential ( $n_{EFW}$ ), respectively, for all intervals in the magnetosheath. The distributions of the  
 970      time shifts (b, d, f, h) of the  $B_z$ , the  $V_X$ , the  $n_{CIS}$  and the  $n_{EFW}$ ), respectively, for all intervals  
 971      in the magnetosheath.



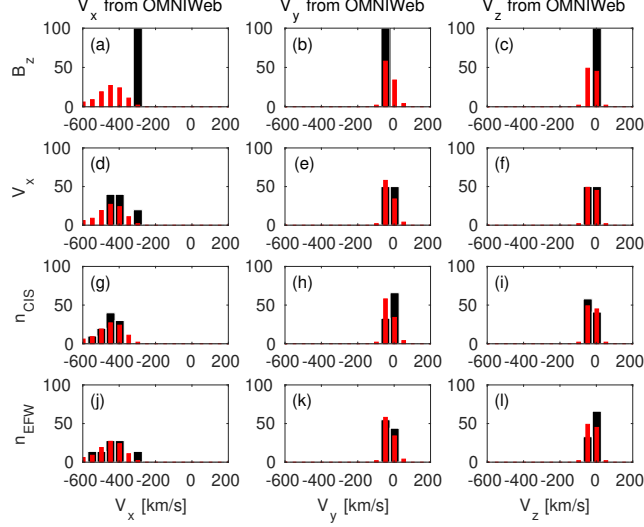
972      **Figure 11.** Cluster SC3 orbit in the magnetosphere in GSE system for all intervals (see Ta-  
973      ble 3). (a) XZ (b) YZ (c) XY (d) Cylindrical projection. Average bow-shock and magnetopause  
974      positions are drawn on all plots using **thick** solid lines [Peredo *et al.*, 1995; Tsyganenko, 1995,  
975      respectively]. The black dots at  $3.7 R_E$  show the boundary of the GUMICS-4 inner magneto-  
976      spheric domain. The black circle in the origo of all plots shows the size of the Earth.



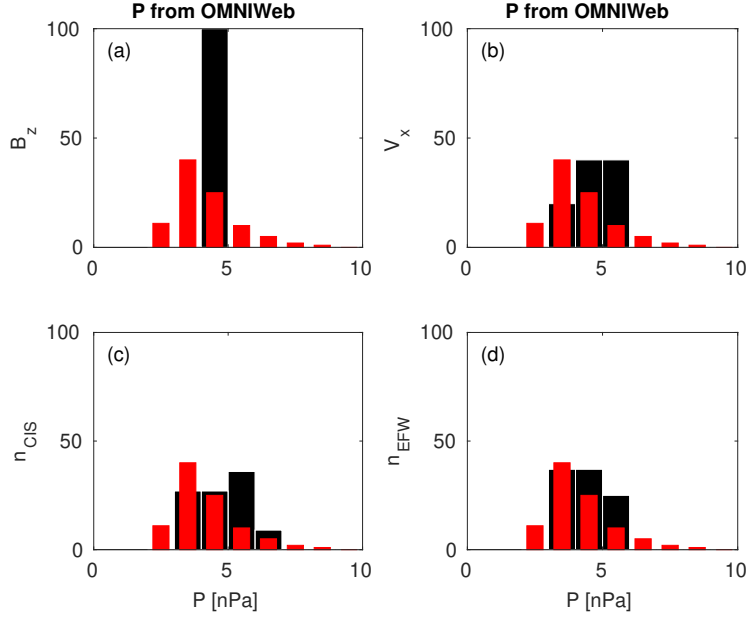
977 **Figure 12.** Cluster SC3 orbit in the tail in GSE system for all intervals (see Table 8). (a) XZ  
 978 (b) YZ (c) XY (d) Cylindrical projection. Average bow-shock and magnetopause positions are  
 979 drawn on all plots using **thick** solid lines [Perez et al., 1995; Tsyganenko, 1995, respectively].  
 980 The black dots at  $3.7 R_E$  show the boundary of the GUMICS-4 inner magnetospheric domain.  
 981 The black circle in the origo of all plots shows the size of the Earth.



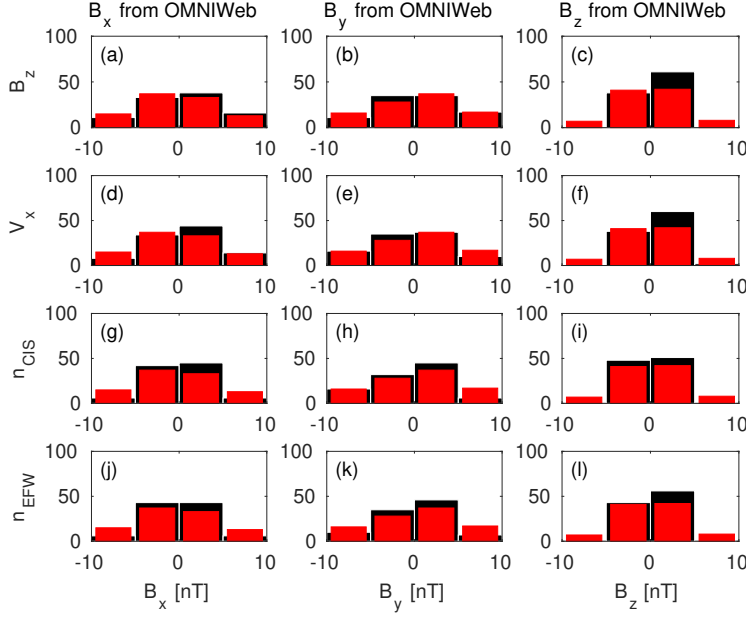
982     **Figure 13.** The **black** distributions of the  $B_x$ , the  $B_y$  and the  $B_z$  OMNI solar wind magnetic  
 983     field components when the agreement of the Cluster SC3 measurements and the GUMICS-4  
 984     simulations are poor in the solar wind (see Table 4). The  $B_z$ , the  $V_x$ , the  $n_{CIS}$  and the  $n_{EFW}$   
 985     are the magnetic field GSE Z component, the plasma ion velocity X GSE component, the solar  
 986     wind density measured by the CIS HIA instrument and the calculated from the EFW spacecraft  
 987     potential, respectively. (a, b, c) Distribution of OMNI  $B_x$ ,  $B_y$ ,  $B_z$  when the agreement of  $B_z$   
 988     is poor. (d, e, f) Distribution of OMNI  $B_x$ ,  $B_y$ ,  $B_z$  when the agreement of  $V_x$  is poor. (g, h, i)  
 989     Distribution of OMNI  $B_x$ ,  $B_y$ ,  $B_z$  when the agreement of  $n_{CIS}$  is poor. (j, k, l) Distribution of  
 990     OMNI  $B_x$ ,  $B_y$ ,  $B_z$  when the agreement of  $n_{EFW}$  is poor. The values are in percentage unit in  
 991     the distributions. **The red distributions of (a, d, g, j), (b, e, h, k) and (c, f, i, l) are**  
 992     **the distribution of the  $B_x$ , the  $B_y$ , and the  $B_z$  components of the OMNI solar wind**  
 993     **magnetic field during the 1-year run from January 29, 2002 to February 2, 2003 in**  
 994     **GSE reference frame, respectively.**



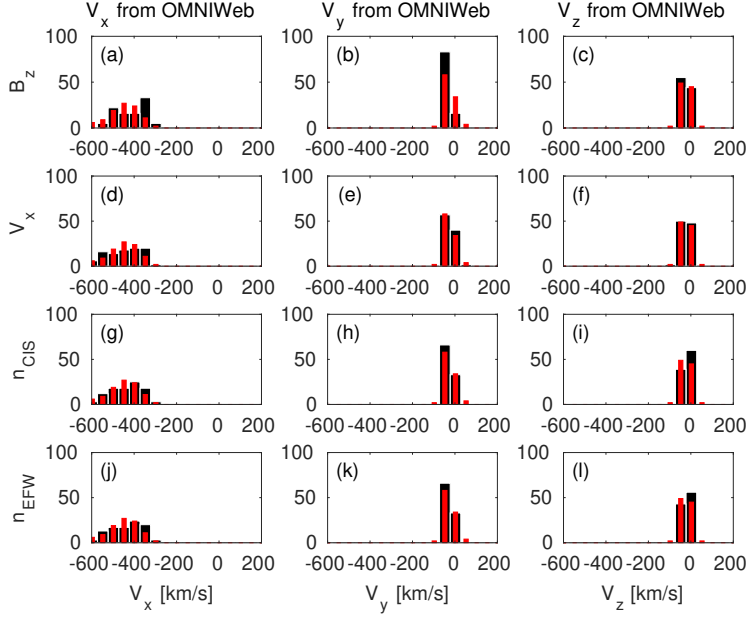
995 **Figure 14.** The **black** distributions of the  $V_x$ , the  $V_y$  and the  $V_z$  OMNI solar wind magnetic  
 996 field components when the agreement of the Cluster SC3 measurements and the GUMICS–4  
 997 simulations are poor in the solar wind (see Table 4). The  $B_z$ , the  $V_x$ , the  $n_{CIS}$  and the  $n_{EFW}$   
 998 are the magnetic field GSE Z component, the plasma ion velocity X GSE component, the solar  
 999 wind density measured by the CIS HIA instrument and the calculated from the EFW spacecraft  
 1000 potential, respectively. (a, b, c) Distribution of OMNI  $V_x$ ,  $V_y$ ,  $V_z$  when the agreement of  $B_z$   
 1001 is poor. (d, e, f) Distribution of OMNI  $V_x$ ,  $V_y$ ,  $V_z$  when the agreement of  $V_x$  is poor. (g, h, i)  
 1002 Distribution of OMNI  $V_x$ ,  $V_y$ ,  $V_z$  when the agreement of  $n_{CIS}$  is poor. (j, k, l) Distribution of  
 1003 OMNI  $V_x$ ,  $V_y$ ,  $V_z$  when the agreement of  $n_{EFW}$  is poor. The values are in percentage unit in  
 1004 the distributions. **The red distributions of (a, d, g, j), (b, e, h, k) and (c, f, i, l) are**  
 1005 **the distributions of the  $V_x$ , the  $V_y$  and the  $V_z$  components of the OMNI solar wind**  
 1006 **velocity during the 1-year run from January 29, 2002 to February 2, 2003 in GSE**  
 1007 **reference frame, respectively.**



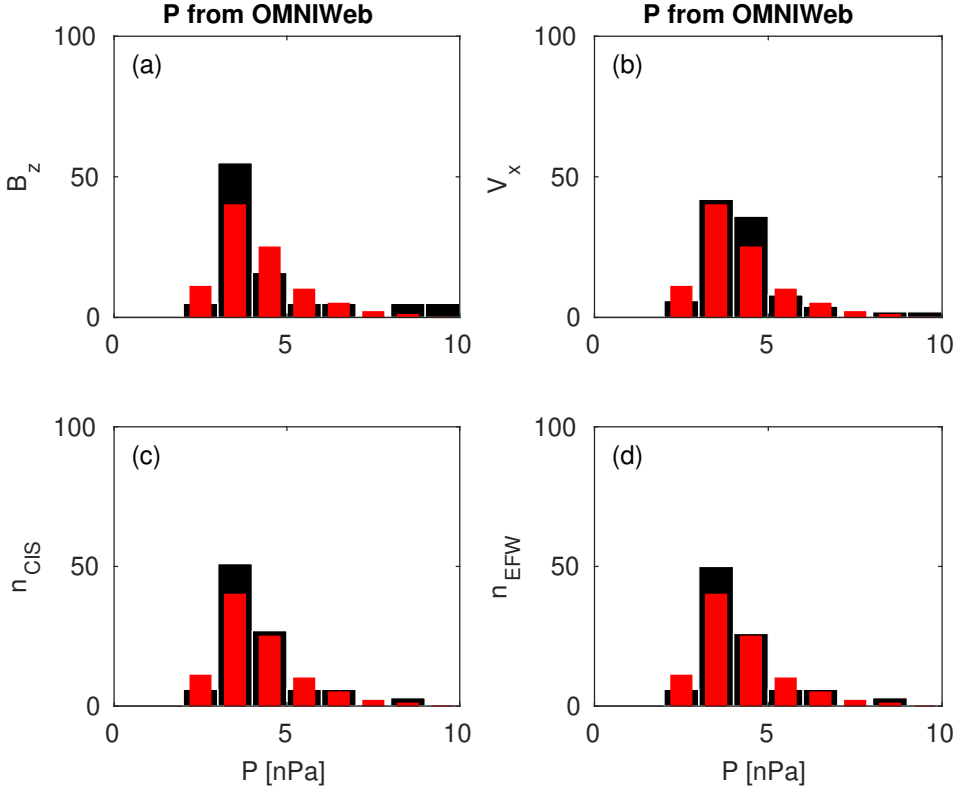
1008      **Figure 15.** The **black** distributions of the  $P$  solar wind dynamic pressure calculated from  
 1009      OMNI parameters when the agreement of the Cluster SC3 measurements and the GUMICS-4  
 1010      simulations are poor in the solar wind (see Table 4). The  $B_z$ ,  $V_x$ ,  $n_{CIS}$  and  $n_{EFW}$  are the mag-  
 1011      netic field GSE Z component, the velocity X GSE component, the solar wind density measured  
 1012      by the CIS HIA instrument and calculated from the EFW spacecraft potential, respectively.  
 1013      (a, b, c, d) The distribution of the  $P$  calculated from OMNI data when the agreement of the  $B_z$ ,  
 1014      the  $V_x$ , the  $n_{CIS}$  or the  $n_{EFW}$  are poor. The values are in percentage unit in the distributions.  
 1015      **The red distributions of (a, b, c, d) are the distributions of the  $P$  solar wind dy-**  
 1016      **namic pressure calculated from the OMNI solar wind parameters during the 1-year**  
 1017      **run from January 29, 2002 to February 2, 2003 in GSE reference frame.**



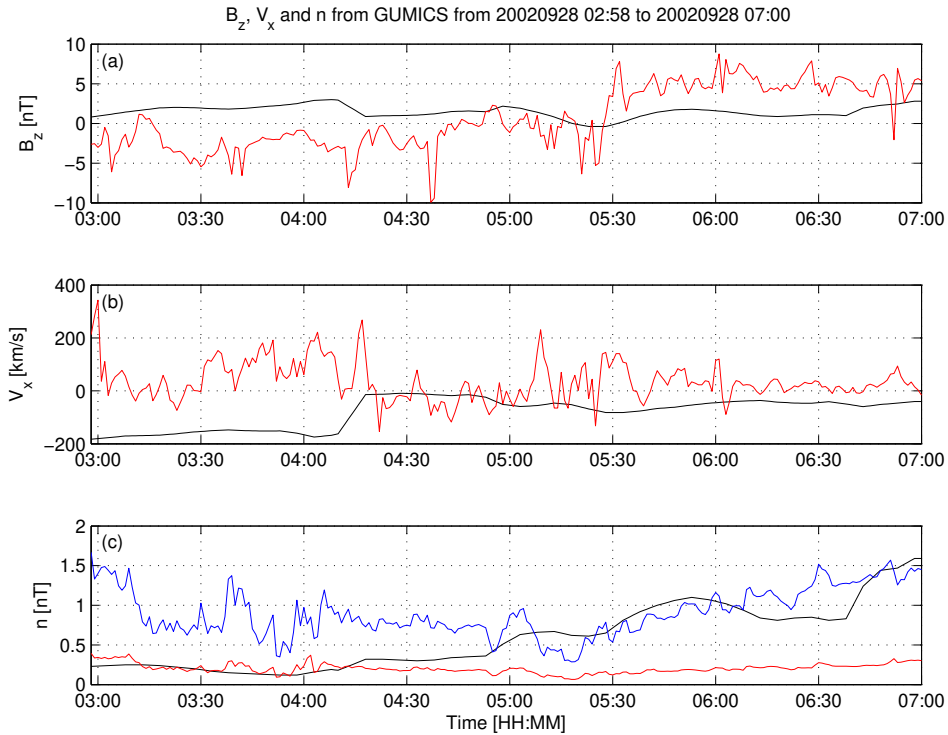
1018 **Figure 16.** The **black** distributions of the  $B_x$ , the  $B_y$  and the  $B_z$  OMNI solar wind magnetic  
 1019 field components when the agreement of the Cluster SC3 measurements and the GUMICS–4  
 1020 simulations are poor in the magnetosheath (see Table 5). The  $B_z$ , the  $V_x$ , the  $n_{CIS}$  and the  
 1021  $n_{EWF}$  are the magnetic field GSE Z component, the plasma ion velocity X GSE component,  
 1022 the solar wind density measured by the CIS HIA instrument and the calculated from the EFW  
 1023 spacecraft potential, respectively. (a, b, c) Distribution of OMNI  $B_x$ ,  $B_y$ ,  $B_z$  when the agree-  
 1024 ment of  $B_z$  is poor. (d, e, f) Distribution of OMNI  $B_x$ ,  $B_y$ ,  $B_z$  when the agreement of  $V_x$  is poor.  
 1025 (g, h, i) Distribution of OMNI  $B_x$ ,  $B_y$ ,  $B_z$  when the agreement of  $n_{CIS}$  is poor. (j, k, l) Distri-  
 1026 bution of OMNI  $B_x$ ,  $B_y$ ,  $B_z$  when the agreement of  $n_{EWF}$  is poor. The values are in percentage  
 1027 unit in the distributions. **The red distributions of (a, d, g, j), (b, e, h, k) and (c, f, i, l)**  
 1028 **are the distribution of the  $B_x$ , the  $B_y$ , and the  $B_z$  components of the OMNI solar**  
 1029 **wind magnetic field during the 1-year run from January 29, 2002 to February 2,**  
 1030 **2003 in GSE reference frame, respectively.**



1031 **Figure 17.** The **black** distributions of the  $V_x$ , the  $V_y$  and the  $V_z$  OMNI solar wind magnetic  
 1032 field components when the agreement of the Cluster SC3 measurements and the GUMICS-4  
 1033 simulations are poor in the magnetosheath (see Table 5). The  $B_z$ , the  $V_x$ , the  $n_{CIS}$  and the  
 1034  $n_{EFW}$  are the magnetic field GSE Z component, the plasma ion velocity X GSE component, the  
 1035 solar wind density measured by the CIS HIA instrument and the calculated from the EFW space-  
 1036 craft potential, respectively. (a, b, c) Distribution of OMNI  $V_x$ ,  $V_y$ ,  $V_z$  when the agreement of  
 1037  $B_z$  is poor. (d, e, f) Distribution of OMNI  $V_x$ ,  $V_y$ ,  $V_z$  when the agreement of  $V_x$  is poor. (g, h, i)  
 1038 Distribution of OMNI  $V_x$ ,  $V_y$ ,  $V_z$  when the agreement of  $n_{CIS}$  is poor. (j, k, l) Distribution of  
 1039 OMNI  $V_x$ ,  $V_y$ ,  $V_z$  when the agreement of  $n_{EFW}$  is poor. The values are in percentage unit in  
 1040 the distributions. **The red distributions of (a, d, g, j), (b, e, h, k) and (c, f, i, l) are**  
 1041 **the distributions of the  $V_x$ , the  $V_y$  and the  $V_z$  components of the OMNI solar wind**  
 1042 **velocity during the 1-year run from January 29, 2002 to February 2, 2003 in GSE**  
 1043 **reference frame, respectively.**



1044      **Figure 18.** The black distributions of the  $P$  solar wind dynamic pressure calculated from  
 1045      OMNI parameters when the agreement of the Cluster SC3 measurements and the GUMICS–4  
 1046      simulations are poor in the magnetosheath (see Table 5). The  $B_z$ ,  $V_x$ ,  $n_{CIS}$  and  $n_{EFW}$  are  
 1047      the magnetic field GSE Z component, the velocity X GSE component, the solar wind density  
 1048      measured by the CIS HIA instrument and calculated from the EFW spacecraft potential, respec-  
 1049      tively. (a, b, c, d) The distribution of the  $P$  calculated from OMNI data when the agreement of  
 1050      the  $B_z$ , the  $V_x$ , the  $n_{CIS}$  or the  $n_{EFW}$  are poor. The values are in percentage unit in the dis-  
 1051      tributions. **The red distributions of (a, b, c, d) are the distributions of the P solar**  
 1052      **wind dynamic pressure calculated from the OMNI solar wind parameters during the**  
 1053      **1-year run from January 29, 2002 to February 2, 2003 in GSE reference frame.**



1054 **Figure 19.** GUMICS-4 simulation results (black) and Cluster SC3 magnetic field Z compo-  
 1055 nent, ion plasma moments (red) and electron density calculated from spacecraft potential (blue)  
 1056 from September 28, 2002 from 2:58 to 7:00 (UT) in the tail in GSE system. (a) Magnetic field  
 1057 Z component. (b) Solar wind velocity X component (c) Solar wind density. From 05:15 to 05:30  
 1058 both the Cluster SC3 and the virtual spaceprobe of the GUMICS-4 simulation cross the neutral  
 1059 sheet multiple times.

Start/End	$C_{B_z}$	$\delta t_{B_z}$	$C_{V_x}$	$\delta t_{V_x}$	$C_{n_{CIS}}$	$\delta t_{n_{CIS}}$	$C_{n_{EFW}}$	$\delta t_{n_{EFW}}$
	[min]		[min]		[min]		[min]	
20020201 20:00/0203 04:00	0.96	2	1.00	13	0.96	3	0.98	3
20020211 13:00/0212 12:00	0.82	2	1.00	0	0.99	18	0.99	18
20020218 09:00/0219 02:00	0.93	0	1.00	-3	0.94	-3	0.97	-3
20020219 06:30/0219 15:00	0.93	1	1.00	0	0.99	-60	1.00	-52
20020220 18:30/0222 00:00	0.87	4	1.00	4	0.93	-21	0.98	3
20020318 17:30/0319 02:30	0.89	1	1.00	21	0.98	50	0.99	5
20020412 20:30/0413 02:00	0.90	4	0.99	-54	0.94	60	0.98	12
20021227 12:00/1228 03:00	0.75	4	1.00	-3	0.99	-26	0.99	21
20021229 20:00/1230 16:00	0.68	1	1.00	1	0.99	-30	0.98	41
20030106 06:00/0106 19:00	0.79	4	1.00	6	0.99	4	0.99	-60
20030108 07:00/0109 03:30	0.55	10	1.00	41	0.99	10	0.97	-55
20030113 08:30/0113 18:00	0.91	3	1.00	5	1.00	3	0.97	-1
20030120 07:30/0120 13:00	0.82	2	1.00	9	1.00	-6	1.00	-3
20030122 12:00/0123 14:00	0.81	2	1.00	3	0.99	3	0.92	-60
20030124 18:00/0126 00:00	0.73	3	1.00	0	0.99	-60	0.99	60
20030127 16:00/0128 06:00	0.88	-1	1.00	-3	0.95	1	0.88	11
20030129 12:00/0130 18:00	0.90	2	1.00	4	0.94	-59	0.98	1

1060 **Table 1.** The studied solar wind intervals. The correlation coefficients ( $C_{B_z}$ ,  $C_{V_x}$ ,  $C_{n_{CIS}}$ ,  
1061  $C_{n_{EFW}}$ ) and time shift ( $\delta t_{V_x}$ ,  $\delta t_{n_{CIS}}$ ,  $\delta t_{n_{EFW}}$ ) in minutes of the magnetic field GSE Z compo-  
1062 nent ( $B_z$ ), solar wind velocity X component ( $V_x$ ), CIS and EFW densities ( $n_{CIS}$ ,  $n_{EFW}$ ).

Table 2: The studied magnetosheath intervals. The correlation coefficients ( $C_{B_z}$ ,  $C_{V_x}$ ,  $C_{n_{CIS}}$ ,  $C_{n_{EFW}}$ ) and time shift ( $\delta t_{V_x}$ ,  $\delta t_{n_{CIS}}$ ,  $\delta t_{n_{EFW}}$ ) in minutes of the magnetic field GSE Z component ( $B_z$ ), solar wind velocity X component ( $V_x$ ), CIS and EFW densities ( $n_{CIS}$ ,  $n_{EFW}$ ). In the empty slots the correlation calculation gives invalid result.

Start/End	$C_{B_z}$	$\delta t_{B_z}$	$C_{V_x}$	$\delta t_{V_x}$	$C_{n_{CIS}}$	$\delta t_{n_{CIS}}$	$C_{n_{EFW}}$	$\delta t_{n_{EFW}}$
		[min]		[min]		[min]		[min]
20020201 13:30/0201 18:30	0.91	1	0.98	56	0.99	60	0.976	60
20020208 18:15/0209 00:00	0.73	2	0.95	60	0.98	-52	0.98	-54
20020211 02:30/0211 09:00	0.79	0	0.99	-20	0.99	-1	0.99	1
20020212 16:30/0212 21:00	0.80	3	0.99	54	0.99	31	0.99	30
20020219 17:30/0219 23:00	0.76	4	0.98	37	0.99	7	0.99	6
20020222 23:00/0223 06:30	0.64	0	0.97	-60	0.99	-47	0.98	-48
20020227 16:30/0227 23:15	0.48	59	0.98	-31	0.99	-39	1.00	-12
20020310 18:30/0311 00:30	0.97	3	0.98	19	0.99	8	0.99	-2
20020311 14:00/0311 19:00	0.86	5	0.97	36	0.99	-3	0.99	-40
20020406 19:00/0407 01:15	0.76	2	0.96	-60	0.98	-55	0.98	-56
20020410 17:30/0410 23:00	0.89	6	0.99	-50	0.99	3	1.00	5
20020411 11:30/0411 16:30	0.82	4	0.99	39	0.99	3	0.99	3
20020418 18:30/0418 22:45	0.92	60	0.99	-60	0.99	60	0.98	60
20020421 04:30/0421 07:45	0.96	47	0.99	-60	1.00	-60	1.00	-60
20020422 11:45/0422 15:45	0.73	-5	0.98	-17	0.99	-15	0.98	-16
20020423 08:30/0423 12:30	0.93	31	0.99	3	0.99	16	0.99	16
20020430 12:30/0430 17:00	0.79	59	0.98	22	0.98	-18		
20020505 07:00/0505 11:15	0.71	59	0.99	-58	0.98	-60		
20020506 19:15/0507 00:15	0.84	-27	0.98	-60	0.97	-37		
20020507 17:30/0507 23:00	0.93	2	0.98	-30	0.99	-49		
20020514 22:45/0515 03:00	0.79	49	0.99	35	0.99	38	0.99	43
20020517 07:00/0517 12:15	0.74	-5	1.00	-5	0.99	-4	0.99	-3
20020518 13:30/0518 19:30	0.70	1	0.99	9	0.97	-1	0.97	-1

*Continued on next page*

Table 2 – *Continued from previous page*

Start/End	$C_{B_z}$	$\delta t_{B_z}$	$C_{V_x}$	$\delta t_{V_x}$	$C_{n_{CIS}}$	$\delta t_{n_{CIS}}$	$C_{n_{EFW}}$	$\delta t_{n_{EFW}}$
		[min]		[min]		[min]		[min]
20020519 20:00/0520 03:30	0.98	2	1.00	-9	0.99	-5	0.99	-50
20020520 10:45/0520 20:15	0.77	1	0.99	-3	0.95	-1	0.99	-1
20020522 02:00/0522 08:45	0.49	52	0.99	4	0.99	12	0.99	22
20020527 02:15/0527 17:15	0.79	-3	0.99	-3	0.98	0	0.98	0
20020530 05:00/0530 10:30	0.29	3	1.00	-38	0.99	3	0.99	3
20020601 19:30/0602 01:00	0.68	-2	1.00	18	0.99	-6	0.99	-7
20020602 21:45/0603 17:45	0.62	-5	0.99	-1	0.98	2	0.99	2
20020605 10:30/0606 06:00	0.18	0	1.00	-7	0.97	10	0.98	9
20020607 18:00/0607 22:00	0.92	-35	1.00	-36	0.99	16	0.99	16
20020608 01:15/0608 18:15	0.53	-4	0.99	-39	0.96	-6	0.97	-6
20020610 01:30/0610 09:30	0.76	5	0.99	8	0.99	-5	0.99	-7
20020610 11:00/0611 01:00	0.87	-4	0.99	-33	0.98	23	0.99	6
20020612 18:30/0613 06:15	0.44	-2	0.99	-7	0.97	4	0.97	-32
20020615 07:00/0615 23:30			1.00	47	0.98	-3	0.98	-3
20020617 05:00/0618 03:45	0.76	4	1.00	28	0.98	10	0.98	8
20020620 04:00/0620 11:00	0.61	-8	0.99	-6	0.97	12	0.98	4
20020622 14:30/0622 18:00	0.98	55	1.00	35	0.99	16	1.00	16
20021201 04:15/1202 07:45	0.38	1	1.00	2	0.99	6	0.99	6
20021203 15:30/1204 19:30	0.67	1	0.99	60	0.98	59	0.98	59
20021207 00:30/1207 07:45	0.49	37	0.98	-56	0.99	-19	0.99	-4
20021208 09:30/1209 08:00	0.69	2	0.98	-35	0.97	6	0.98	4
20021212 23:30/1213 14:30	0.51	5	1.00	36	0.99	-3	0.81	-56
20021213 21:15/1214 09:30	0.93	5	0.99	-35	0.99	-13	0.99	-47
20021215 12:45/1216 18:00	0.76	2	0.99	-60	0.94	-60	0.98	31
20021217 16:30/1218 01:45	0.99	2	1.00	-54	0.99	3	0.99	3
20021220 01:30/1220 06:15	0.92	0	1.00	60	0.99	2	0.99	3
20021223 02:15/1223 13:00	0.91	1	0.97	49	0.93	49	0.99	-14
20021223 14:00/1223 22:30	0.84	1	0.99	-2	0.99	-1	1.00	-3
20021224 19:00/1225 01:45	0.94	0	1.00	-44	0.99	26	0.99	27

*Continued on next page*

Table 2 – *Continued from previous page*

Start/End	$C_{B_z}$	$\delta t_{B_z}$	$C_{V_x}$	$\delta t_{V_x}$	$C_{n_{CIS}}$	$\delta t_{n_{CIS}}$	$C_{n_{EFW}}$	$\delta t_{n_{EFW}}$
		[min]		[min]		[min]		[min]
20021225 23:45/1226 07:15	0.96	7	1.00	-17	0.99	56	0.99	55
20021226 23:00/1227 09:45	0.79	2	1.00	2	0.98	4	0.99	3
20021229 11:45/1229 17:00	0.60	2	1.00	-60	0.98	-19	0.98	50
20021230 17:45/1231 01:00	0.69	1	0.98	52	0.98	60	0.98	22
20021231 23:00/0101 05:15	0.89	2	0.99	15	0.99	-54	1.00	-58
20030105 14:00/0105 21:00	0.69	0	0.99	1	0.98	-60	0.99	-60
20030106 23:15/0107 03:00	0.52	9	0.98	60	0.99	56	1.00	-60
20030109 08:45/0109 16:15			0.91	-56	0.98	-13	0.98	-26
20030110 07:15/0110 15:15	0.94	1	0.99	-7	0.99	1	0.98	5
20030111 08:15/0111 22:30	0.84	0	0.99	-59	0.94	-15	0.94	8
20030112 17:30/0113 00:15	0.98	0	1.00	-52	0.99	39	0.99	51
20030114 00:30/0114 08:30	0.84	-1	0.99	-60	0.98	23	0.98	8
20030116 10:15/0116 17:45	0.62	60	0.93	52	0.99	60	0.99	30
20030117 09:30/0117 13:30	0.68	-3	1.00	8	1.00	-31	0.99	-33
20030118 23:30/0119 03:45	0.93	3	1.00	-12	1.00	7	0.99	7
20030119 21:00/0120 01:00	0.94	3	1.00	5	1.00	38	1.00	19
20030121 06:30/0121 11:30	0.82	-15	0.96	47	0.98	7	0.99	-39
20030122 04:45/0122 09:30	0.69	-2	1.00	10	0.99	-9	0.99	-5
20030126 01:45/0126 06:30	0.85	3	0.99	-15	0.99	-50	0.99	23
20030127 08:15/0127 13:00	1.00	9	1.00	-60	0.98	0	0.99	1
20030128 12:30/0128 17:15	0.77	60	0.99	-24	0.99	-6	0.988	20
20030130 19:45/0131 00:15	0.98	2	0.99	51	0.99	25	0.99	9

Table 3: The studied magnetosphere intervals (UT).

Start/End
20020213 23:00/0214 01:30
20020217 18:30/0218 02:00
20020220 00:45/0220 12:00
20020222 11:15/0222 20:15
20020225 02:15/0225 08:30
20020227 06:00/0227 12:00
20020302 00:00/0302 03:15
20020306 10:00/0306 18:30
20020308 17:30/0309 06:00
20020311 02:15/0311 12:00
20020313 11:15/0314 00:15
20020316 04:45/0316 08:00
20020318 09:00/0318 14:45
20020320 20:30/0320 23:55
20020323 04:00/0323 09:45
20020327 23:45/0328 06:15
20020330 07:15/0330 12:45
20020401 19:30/0401 22:00
20020406 09:30/0406 18:00
20020408 15:00/0409 00:00
20020410 23:30/0411 09:45
20020413 08:30/0413 19:00
20020416 18:00/0417 04:30
20020418 06:00/0418 12:00
20020420 15:00/0420 23:00
20020422 20:00/0423 07:00
20020425 08:30/0425 18:00
20020430 04:40/0430 12:00
20020504 14:30/0504 16:45

*Continued on next page*

Table 3 – *Continued from previous page*

Start/End
20020505 02:30/0505 07:00
20020507 01:30/0507 15:45
20020508 11:00/0510 04:15
20020512 02:45/0512 09:30
20020514 10:30/0514 12:45
20020519 00:30/0519 19:30
20020521 01:30/0521 22:00
20020523 23:30/0524 02:00
20020524 19:00/0525 08:15
20020526 07:30/0526 10:30
20020528 20:00/0529 05:00
20020531 02:15/0531 13:30
20020602 04:30/0602 07:30
20020602 12:00/0602 21:30
20020604 08:30/0605 07:00
20020606 14:30/0607 16:30
20020609 06:00/0609 20:00
20020611 11:00/0612 13:00
20020614 01:00/0614 16:00
20020616 08:00/0616 18:00
20020620 13:30/0622 01:00
20020623 13:00/0623 17:00
20020624 04:00/0624 10:15
20020630 17:45/0701 15:00
20020701 21:00/0703 10:30
20020703 23:00/0706 03:15
20020707 01:00/0708 23:00
20020710 11:30/0714 03:30
20020714 15:45/0715 15:30
20020716 23:30/0717 16:00

*Continued on next page*

Table 3 – *Continued from previous page*

Start/End
20020718 05:45/0722 11:00
20020722 23:45/0728 01:00
20020728 02:00/0804 03:45
20020804 04:45/0811 06:15
20020811 07:30/0816 01:00
20020816 15:30/0818 09:00
20020818 10:00/0825 11:30
20020825 13:00/0901 14:15
20020901 17:15/0903 23:30
20020905 02:15/0906 16:30
20020907 10:30/0908 17:00
20020908 18:00/0915 19:30
20020915 21:00/0922 22:30
20020923 00:00/0923 23:30
20020924 03:30/0928 22:45
20020928 23:30/0930 01:00
20020930 02:15/1006 17:00
20021006 17:45/1007 03:30
20021007 05:00/1007 17:30
20021008 07:30/1010 22:00
20021010 22:30/1012 22:30
20021012 23:00/1014 06:30
20021014 09:00/1016 04:00
20021016 14:00/1019 00:15
20021019 01:30/1019 22:00
20021021 04:00/1022 19:30
20021022 22:30/1026 02:30
20021026 04:00/1029 20:15
20021030 01:30/1102 08:00
20021102 22:00/1104 22:00

*Continued on next page*

Table 3 – *Continued from previous page*

Start/End
20021106 00:00/1107 18:00
20021108 02:00/1109 18:45
20021111 00:00/1112 01:30
20021113 03:45/1114 14:15
20021115 20:30/1116 23:00
20021118 01:00/1118 23:30
20021120 17:00/1121 06:00
20021122 21:30/1124 01:00
20021125 04:00/1126 08:30
20021127 20:00/1128 18:30
20021130 04:00/1201 01:30
20021202 14:30/1203 09:00
20021204 22:00/1205 19:30
20021207 09:00/1207 16:30
20021207 18:00/1207 22:00
20021209 16:30/1210 14:30
20021212 13:45/1212 21:30
20021214 13:30/1214 20:00
20021214 21:00/1215 07:30
20021216 21:00/1217 15:00
20021219 08:00/1219 19:30
20021221 15:45/1221 23:15
20021222 00:30/1222 08:45
20021224 02:30/1224 14:00
20021226 10:00/1226 19:00
20021228 19:30/1229 02:30
20021229 04:00/1229 10:00
20021231 05:00/1231 18:45
20030102 12:30/0102 20:45
20030104 20:45/0105 06:00

*Continued on next page*

Table 3 – *Continued from previous page*

Start/End
20030105 07:00/0105 13:30
20030107 05:45/0107 21:00
20030109 17:00/0110 00:45
20030112 00:00/0112 09:15
20030112 10:30/0112 16:00
20030114 11:00/0114 20:00
20030116 20:30/0116 22:45
20030119 04:30/0119 09:30
20030119 14:00/0119 17:00
20030121 13:30/0121 21:30
20030126 07:30/0126 15:45
20030128 17:45/0129 08:15
20030131 01:30/0131 11:45

Start/End	OMNI			Cluster SC3			
	$B_z$ [nT]	$V_x$ [km/s]	P [cm $^{-3}$ ]	$B_z$	$V_x$	$n_{CIS}$	$n_{EFW}$
20020201 20:00/0203 04:00	-1.25	-373.52	4.08	y	y	n	y
20020211 13:00/0212 12:00	0.03	-533.11	2.18	y	y	y	y
20020218 09:00/0219 02:00	2.56	-362.41	3.46	y	n	n	y
20020219 06:30/0219 15:00	3.55	-401.63	1.25	y	y	n	n
20020220 18:30/0222 00:00	1.95	-440.18	1.96	y	y	n	y
20020318 17:30/0319 02:30	3.79	-429.30	15.34	y	n	n	n
20020412 20:30/0413 02:00	-1.81	-420.35	3.24	y	n	n	y
20021227 12:00/1228 03:00	0.09	-714.40	2.72	y	n	n	y
20021229 20:00/1230 16:00	-0.37	-526.40	2.26	y	y	n	n
20030106 06:00/0106 19:00	2.25	-399.91	1.50	y	n	n	n
20030108 07:00/0109 03:30	-0.58	-280.80	2.97	n	n	y	n
20030113 08:30/0113 18:00	0.68	-397.83	1.72	y	y	y	n
20030120 07:30/0120 13:00	2.16	-630.69	2.43	y	y	y	y
20030122 12:00/0123 14:00	0.13	-608.96	3.41	y	y	y	n
20030124 18:00/0126 00:00	-0.71	-739.68	2.87	y	y	n	n
20030127 16:00/0128 06:00	-0.92	-451.84	3.12	y	y	n	n
20030129 12:00/0130 18:00	-3.09	-450.00	3.96	y	y	n	y

1065 **Table 4.** The average OMNI input parameters in the solar wind and the good/bad agreement  
 1066 of the GUMICS–4 simulations to the Cluster  $B_z$  magnetic field component, the  $V_x$  solar wind  
 1067 speed component, the  $n_{CIS}$  solar wind density measured by the Cluster CIS HIA instrument and  
 1068 the  $n_{EFW}$  solar wind density calculated from the spacecraft potential measured by the Cluster  
 1069 EFW instrument in the solar wind.

Table 5: The average OMNI input parameters in the solar wind and the good/bad agreement of the GUMICS–4 simulations to the Cluster  $B_z$  magnetic field component, the  $V_x$  solar wind speed component, the  $n_{CIS}$  solar wind density measured by the Cluster CIS HIA instrument and the  $n_{EFW}$  solar wind density calculated from the spacecraft potential measured by the Cluster EFW instrument in the magnetosheath.

Start/End	OMNI			Cluster SC3			
	$B_z$	$V_x$	P	$B_z$	$V_x$	$n_{CIS}$	$n_{EFW}$
	[nT]	[km/s]	[cm $^{-3}$ ]				
20020201 13:30/0201 18:30	0.19	-342.87	4.62	y	n	n	n
20020208 18:15/0209 00:00	-0.48	-508.16	1.61	y	n	n	n
20020211 02:30/0211 09:00	-1.85	-425.67	1.78	y	y	y	y
20020212 16:30/0212 21:00	2.98	-509.22	2.34	y	n	n	n
20020219 17:30/0219 23:00	1.46	-431.50	1.46	y	y	y	y
20020222 23:00/0223 06:30	0.86	-391.22	1.14	y	n	n	n
20020227 16:30/0227 23:15	1.89	-343.13	1.52	n	n	n	n
20020310 18:30/0311 00:30	-2.81	-379.46	1.78	y	y	y	y
20020311 14:00/0311 19:00	1.63	-371.43	2.68	n	n	n	n
20020406 19:00/0407 01:15	-2.71	-333.13	0.93	y	n	n	n
20020410 17:30/0410 23:00	0.31	-312.43	4.42	n	n	y	y
20020411 11:30/0411 16:30	-1.50	-494.02	4.25	y	y	n	n
20020418 18:30/0418 22:45	-0.92	-450.82	0.30	n	n	n	n
20020421 04:30/0421 07:45	0.40	-455.69	1.37	n	n	n	n
20020422 11:45/0422 15:45	0.25	-419.98	1.14	n	n	y	y
20020423 08:30/0423 12:30	2.77	-507.99	6.82	n	n	n	n
20020430 12:30/0430 17:00	2.15	-479.51	3.02	n	n	n	n
20020505 07:00/0505 11:15	0.20	-336.81	1.74	n	n	n	n
20020506 19:15/0507 00:15	0.78	-390.00	2.46	y	n	n	n
20020507 17:30/0507 23:00	2.87	-392.40	3.49	y	n	n	n
20020514 22:45/0515 03:00	-2.42	-414.01	1.82	n	n	n	n

*Continued on next page*

Table 5 – *Continued from previous page*

Start/End	OMNI			Cluster SC3			
	$B_z$ [nT]	$V_x$ [km/s]	P $[cm^{-3}]$	$B_z$	$V_x$	$n_{CIS}$	$n_{EFW}$
20020517 07:00/0517 12:15	-0.39	-379.32	1.52	y	y	y	y
20020518 13:30/0518 19:30	0.63	-345.87	1.59	n	n	y	y
20020519 20:00/0520 03:30	4.75	-408.56	1.12	y	y	y	y
20020520 10:45/0520 20:15	0.74	-448.89	1.93	y	y	y	y
20020522 02:00/0522 08:45	-1.07	-398.12	1.63	n	y	y	y
20020527 02:15/0527 17:15	-3.11	-542.53	2.07	y	y	y	y
20020530 05:00/0530 10:30	0.03	-493.86	2.08	y	n	y	y
20020601 19:30/0602 01:00	-3.38	-342.27	4.16	y	y	y	y
20020602 21:45/0603 17:45	0.38	-435.47	1.89	y	y	y	y
20020605 10:30/0606 06:00	-0.42	-394.49	1.08	y	y	n	n
20020607 18:00/0607 22:00	-1.60	-291.85	1.80	y	y	y	y
20020608 01:15/0608 18:15	0.06	-335.39	2.74	y	n	y	y
20020610 01:30/0610 09:30	1.60	-465.52	3.00	y	y	y	y
20020610 11:00/0611 01:00	-2.27	-419.86	2.16	y	n	y	y
20020612 18:30/0613 06:15	-1.13	-351.03	1.16	y	y	y	y
20020615 07:00/0615 23:30	-1.16	-334.27	2.84	n	n	y	y
20020617 05:00/0618 03:45	0.78	-351.47	1.87	y	n	y	y
20020620 04:00/0620 11:00	0.46	-485.48	1.73	y	y	y	y
20020622 14:30/0622 18:00	-0.72	-429.02	1.93	n	n	y	y
20021201 04:15/1202 07:45	-1.09	-499.23	2.62	y	y	y	y
20021203 15:30/1204 19:30	0.34	-449.09	2.06	y	n	n	n
20021207 00:30/1207 07:45	0.80	-451.80	7.33	n	n	y	y
20021208 09:30/1209 08:00	0.60	-600.27	1.49	y	n	y	y
20021212 23:30/1213 14:30	0.10	-337.77	1.32	y	n	n	n
20021213 21:15/1214 09:30	-0.74	-361.19	2.99	y	n	y	y
20021215 12:45/1216 18:00	1.32	-479.48	1.53	y	n	n	n
20021217 16:30/1218 01:45	4.56	-393.99	2.49	y	n	y	y
20021220 01:30/1220 06:15	-1.21	-530.62	3.01	y	n	y	y

*Continued on next page*

Table 5 – *Continued from previous page*

Start/End	OMNI			Cluster SC3			
	$B_z$ [nT]	$V_x$ [km/s]	P $[cm^{-3}]$	$B_z$	$V_x$	$n_{CIS}$	$n_{EFW}$
20021223 02:15/1223 13:00	-2.32	-516.12	2.22	y	n	n	n
20021223 14:00/1223 22:30	0.89	-519.77	2.55	y	y	y	y
20021224 19:00/1225 01:45	0.88	-523.86	3.41	y	n	y	y
20021225 23:45/1226 07:15	-0.61	-414.38	2.21	y	y	n	n
20021226 23:00/1227 09:45	-1.79	-618.14	6.20	y	y	y	y
20021229 11:45/1229 17:00	-0.41	-580.12	2.39	y	n	n	n
20021230 17:45/1231 01:00	-1.01	-483.60	1.93	y	n	n	y
20021231 23:00/0101 05:15	0.60	-418.95	1.94	y	n	n	n
20030105 14:00/0105 21:00	-0.03	-414.46	1.69	y	n	n	n
20030106 23:15/0107 03:00	-1.62	-392.29	1.56	n	n	n	n
20030109 08:45/0109 16:15	1.45	-272.82	2.31	n	n	n	n
20030110 07:15/0110 15:15	-2.11	-401.03	2.72	y	n	y	y
20030111 08:15/0111 22:30	-0.20	-433.33	1.24	y	n	n	y
20030112 17:30/0113 00:15	1.53	-389.62	1.45	y	n	n	n
20030114 00:30/0114 08:30	-1.67	-388.53	2.27	y	n	n	y
20030116 10:15/0116 17:45	-1.20	-328.91	1.22	n	n	n	n
20030117 09:30/0117 13:30	-1.36	-327.09	2.55	y	y	y	y
20030118 23:30/0119 03:45	6.41	-459.46	4.82	y	y	y	y
20030119 21:00/0120 01:00	1.52	-597.95	2.38	y	n	y	y
20030121 06:30/0121 11:30	-1.77	-670.25	1.50	y	n	n	n
20030122 04:45/0122 09:30	0.11	-588.87	2.30	y	n	y	y
20030126 01:45/0126 06:30	-0.24	-713.82	2.75	y	y	y	y
20030127 08:15/0127 13:00	7.94	-509.30	0.47	y	n	y	y
20030128 12:30/0128 17:15	4.95	-443.83	4.15	y	y	y	y
20030130 19:45/0131 00:15	4.21	-510.33	2.63	y	n	y	y

Table 6: Intervals around the studied bow shock crossings. The Cluster SC3 crossed the bow shock in all cases. The 2nd column shows whether the bow shock is visible in the GUMICS–4 simulations.

Start/End	GUMICS Bow Shock
20020201 12:00/0202 00:00	+
20020203 00:00/0203 12:00	+
20020206 06:00/0206 18:00	+
20020208 18:00/0209 06:00	+
20020211 06:00/0211 18:00	+
20020212 12:00/0212 18:00	+
20020213 12:00/0213 18:00	+
20020216 00:00/0216 12:00	+
20020217 06:00/0217 12:00	-
20020218 06:00/0218 18:00	+
20020219 00:00/0219 18:00	+
20020220 12:00/0221 00:00	+
20020221 18:00/0222 00:00	+
20020301 06:00/0301 12:00	+
20020304 12:00/0304 18:00	+
20020306 00:00/0306 06:00	+
20020307 00:00/0307 06:00	+
20020308 06:00/0308 12:00	+
20020309 06:00/0309 12:00	+
20020310 12:00/0311 00:00	+
20020311 18:00/0312 00:00	+
20020313 00:00/0313 06:00	-
20020314 00:00/0314 12:00	+
20020316 06:00/0316 18:00	+
20020318 12:00/0319 00:00	+
20020323 12:00/0323 18:00	+

*Continued on next page*

Table 6 – *Continued from previous page*

Start/End	GUMICS Bow Shock
20020325 18:00/0326 06:00	–
20020327 06:00/0327 12:00	+
20020329 18:00/0330 00:00	–
20020402 00:00/0402 06:00	+
20020405 18:00/0406 00:00	–
20020407 00:00/0407 06:00	–
20020409 06:00/0409 12:00	–
20020410 12:00/0410 18:00	–
20020411 12:00/0411 18:00	–
20020413 00:00/0413 06:00	+
20020413 18:00/0414 06:00	+
20020420 00:00/0420 06:00	+
20020423 12:00/0423 23:00	+
20020427 00:00/0427 06:00	+
20020428 06:00/0428 12:00	+
20020430 18:00/0501 00:00	+
20020505 06:00/0505 18:00	–
20020507 18:00/0509 06:00	+
20020510 06:00/0510 12:00	+
20020513 12:00/0513 18:00	+
20020515 00:00/0515 06:00	–
20020520 00:00/0520 06:00	+
20020522 06:00/0522 12:00	+
20020522 18:00/0523 06:00	+
20021206 06:00/1207 06:00	+
20021218 00:00/1219 00:00	+
20021220 18:00/1221 00:00	+
20021221 00:00/1221 12:00	+
20021222 12:00/1223 00:00	+
20021223 00:00/1223 06:00	+

*Continued on next page*

Table 6 – *Continued from previous page*

Start/End	GUMICS Bow Shock
20021225 06:00/1226 00:00	+
20021227 06:00/1228 00:00	+
20021228 00:00/1228 12:00	+
20021229 12:00/1230 00:00	+
20030101 06:00/0102 00:00	+
20030103 06:00/0103 12:00	+
20030104 00:00/0104 18:00	+
20030106 00:00/0107 00:00	+
20030108 00:00/0108 12:00	+
20030113 00:00/0114 06:00	+
20030115 00:00/0115 12:00	+
20030118 18:00/0119 00:00	+
20030120 00:00/0121 12:00	+
20030122 06:00/0122 12:00	+
20030123 12:00/0124 00:00	+
20030124 12:00/0124 18:00	+
20030126 00:00/0126 06:00	+
20030127 00:00/0127 18:00	+
20030128 06:00/0128 18:00	+
20030129 06:00/0129 12:00	+
20030130 18:00/0131 00:00	+

Table 7: Intervals around the studied magnetopause crossings.  
The Cluster SC3 crossed the magnetopause in all cases. The  
2nd column shows whether the magnetopause is visible in the  
GUMICS–4 simulations.

Start/End	GUMICS Magnetopause
20020203 06:00/0203 12:00	+
20020206 06:00/0206 12:00	-
20020211 00:00/0211 06:00	+
20020218 00:00/0218 06:00	+
20020225 06:00/0225 12:00	+
20020302 00:00/0302 06:00	+
20020306 18:00/0307 00:00	-
20020308 12:00/0308 18:00	-
20020311 12:00/0311 18:00	+
20020313 18:00/0314 00:00	-
20020314 00:00/0314 06:00	+
20020323 06:00/0323 12:00	+
20020330 12:00/0330 18:00	-
20020404 06:00/0404 12:00	-
20020409 00:00/0409 06:00	-
20020418 12:00/0418 18:00	+
20020422 12:00/0422 18:00	-
20020429 18:00/0430 00:00	-
20020507 12:00/0507 18:00	-
20020509 06:00/0509 12:00	-
20020510 00:00/0510 06:00	-
20020514 18:00/0515 00:00	-
20020519 12:00/0519 18:00	-
20020520 12:00/0521 00:00	-
20020522 00:00/0522 06:00	-
20020529 00:00/0529 12:00	-

*Continued on next page*

Table 7 – *Continued from previous page*

Start/End	GUMICS Magnetopause
20020530 06:00/0530 18:00	–
20020531 18:00/0601 00:00	–
20020602 18:00/0603 00:00	–
20020604 06:00/0604 12:00	–
20020605 06:00/0606 18:00	–
20020607 12:00/0608 06:00	+
20020609 00:00/0609 06:00	–
20020610 00:00/0610 06:00	–
20020611 00:00/0611 12:00	–
20020612 06:00/0614 00:00	–
20020614 18:00/0615 06:00	–
20020616 00:00/0616 12:00	+
20020620 00:00/0620 18:00	–
20020622 06:00/0622 18:00	–
20020704 12:00/0705 00:00	–
20020706 00:00/0706 12:00	+
20020709 00:00/0709 18:00	–
20020715 18:00/0716 12:00	–
20030105 06:00/0105 18:00	+
20030110 00:00/0110 12:00	+
20030112 12:00/0112 18:00	–
20030117 06:00/0117 12:00	+
20030121 06:00/0121 12:00	+
20030122 00:00/0122 06:00	–
20030126 18:00/0127 00:00	+
20030128 12:00/0128 18:00	+
20030129 00:00/0129 12:00	+
20030131 12:00/0201 00:00	+

Start/End	GUMICS Neutral Sheet
20020901 19:10/0901 23:54	–
20020906 14:07/0906 16:37	+
20020913 17:33/0913 20:06	+
20020918 12:47/0918 14:26	–
20020920 20:36/0921 02:13	+
20020928 02:58/0928 07:00	+
20021002 16:12/1002 23:52	–
20021014 12:34/1014 22:53	+
20021017 03:08/1017 04:11	–

<sup>1073</sup> **Table 8.** Intervals around the studied neutral sheet crossings in the tail. The Cluster SC3  
<sup>1074</sup> crossed the neutral sheet in all cases. The 2nd column shows whether the neutral sheet is visible  
<sup>1075</sup> in the GUMICS–4 simulations.